UNIVERSITY OF BIRMINGHAM

University of Birmingham
Research at Birmingham

Variable operation of a renewable energy-driven reverse osmosis system using model predictive control and variable recovery

Mito, Mohamed T.; Ma, Xianghong; Albuflasa, Hanan; Davies, Philip

[Link to publication on Research at Birmingham portal](#)

Variable operation of a renewable energy-driven reverse osmosis system using model predictive control and variable recovery: Towards large-scale implementation

Mohamed T. Mito [a,d], Xianghong Ma [a], Hanan Albuflasa [b], Philip A. Davies [c,*]

[a] Sustainable Environment Research Group, School of Engineering and Technology, Aston University, Birmingham B4 7ET, UK
[b] Department of Physics, College of Science, University of Bahrain, P O Box 32038, Bahrain
[c] School of Engineering, University of Birmingham, Edgbaston, Birmingham B15 2TT, UK
[d] Mechanical Engineering Department, College of Engineering and Technology, Arab Academy for Science, Technology and Maritime Transport, Abu-Qir, Alexandria, Egypt

HIGHLIGHTS

- The integration of reverse osmosis (RO) systems and renewable energy is investigated.
- A control system suitable for variable operation of large-scale RO plants is developed.
- Model predictive control (MPC) is compared to a proportional-integral (PI) controller.
- Operation at variable recovery is optimum for RO plants using a variable power input.
- MPC improves permeate production by 2.35% for a defined power input time-series.

ARTICLE INFO

ABSTRACT

Powering Reverse Osmosis (RO) systems with Renewable Energy (RE) is essential for decarbonising water production. Integration of RE requires large-scale RO plants to operate efficiently using variable power. Nevertheless, variable operation (involving matching the RO load to available power without battery back-up) has only been implemented for small-scale systems. This paper presents a variable-speed operation technique suitable for large-scale RO systems using an optimised operational strategy and a Model Predictive Controller (MPC). The technique was validated using a laboratory test rig having comparable performance to large-scale systems. A dynamic plant model was used to design the operational strategy and control system. Several operational strategies were explored for varying the operating parameters according to power available from a RE source. An advanced control system based on MPC was designed and compared to a conventional Proportional-Integral-Differential controller. The results showed that operation at variable recovery with constant brine flowrate delivered the lowest specific energy consumption and widest operation range for a system with an isobaric pressure exchanger. The MPC controller improved the settling time for a 10% step-change in permeate flowrate by 47%. Moreover, it improved energy utilisation, giving a 2.35% increase in hourly permeate production for a defined power input time-series.

1. Introduction

Water scarcity is affecting more than 40% of the global population and the situation is expected to worsen with growing water demand [1,2]. Desalination is an increasingly viable solution to meet rising demand from the municipal, industrial and agricultural sectors [3]. Since 2010, the desalination industry has grown consistently at a rate of 5 to 6% per year to keep up with such demand [4]. Reverse osmosis (RO) has become the dominant desalination technology due to its simplicity and high energy efficiency. By 2016, 65% of global desalination capacity consisted of RO [5,6]. However, the dependency of RO on fossil fuels and its impact on the environment is causing concern. The CO_2 emission from seawater RO plants is estimated to range from 1.7 to 2.8 kgCO_2 per

Nomenclature

Symbols

A_m	active area, m^2
A_w	water transport coefficient, m/bar.s
B_s	salt transport coefficient, m/s
C	concentration, kg/m^3
$C_{p,m}$	local permeate concentration, kg/m^3
C_v	valve flow coefficient, m^3/s
D_B	brine diffusivity, m^2/s
d	module diameter, m
d_h	hydraulic diameter, m
F	motor frequency, Hz
H_c	control horizon
H_p	prediction horizon
J_w	water flux, m/s
J_s	salt flux, kg/s m^2
K_m	mass transfer coefficient, m/s
K_d	differential controller gain
K_i	integral controller gain
K_p	proportional controller gain
k	sampling time
l_{bc}	membrane length, m
MW	molecular weight, 58.44 kg/kmol
N	rotational speed, rpm
N_p	number of poles of a motor
N_{pv}	number of pressure vessels
n_e	number of modules per pressure vessel
n_i	number of moles
n_l	number of membrane leaves
P	pressure, bar
P_{drop}	pressure drop, bar
P_e	electric power, kW
P_{shaft}	shaft power, kW
P_w	wind power, kW
Q	volumetric flowrate, m^3/s
R	universal gas constant, 8.3144×10^{-2} m^3 bar/K kmol
Re	Reynolds number
$Rec.$	recovery, %
Sc	Schmidt number
SG	seawater specific gravity
Sh	Sherwood number
T	temperature, °C
TCF	temperature correction factor
t	time, s
t_{bc}	brine channel thickness, m
t_{pc}	permeate channel thickness, m

t_{sp}	feed-spacer thickness, m
u	manipulated input
V_{bc}	brine channel volume, m^3
V_{bulk}	bulk flow velocity, m/s
V_d	volumetric displacement, m^3/rev
V_{pc}	permeate channel volume, m^3
V_{ws}	wind speed, m/s
w_{bc}	membrane width, m
y	controlled output
ΔP	differential pressure, bar
ϕ_{bc}	brine channel void fraction
η_m	motor efficiency
η_p	pump efficiency
μ	viscosity, Pa.s
π	osmotic pressure, bar
ρ	density, kg/m^3
τ	torque, N.m
ω	rotational velocity, rad/s

Acronyms

ERD	energy recovery device
FT	flow transmitter
HPP	high-pressure pump
LPP	low-pressure pump
MPC	model predictive control
PID	proportional-integral-differential control
PV	pressure vessel
RE	renewable energy
RO	reverse osmosis
RMSE	root mean square error
SEC	specific energy consumption
VFD	variable frequency drive

Subscripts

b	brine stream
$bulk$	bulk stream
f	feed stream
HPP	relating to the high-pressure pump
$iSave$	relating to the energy recovery device
LPP	relating to the low-pressure pump
Lub	lubrication stream
p	permeate stream
ref	reference value
$shaft$	shaft
$total$	total
w	membrane wall

m^3 of water produced, thus having a significant environmental impact given the large-scale operation of RO [7]. Meanwhile, the improvement in energy-efficiency of RO systems has tended to reach a plateau, as the technology gradually approaches the ideal minimum Specific Energy Consumption (SEC) and as the main components reach technological maturity [4,8].

Renewable Energy (RE) is a promising alternative that can decarbonize water production by RO. RE can produce water at a comparable price to fossil-fuelled systems with much lower emissions; and its feasibility is expected to improve further with the steadily declining price of RE [9]. However, RE fluctuation and intermittency are major drawbacks for deployment in large-scale RO systems (i.e. plants with production capacity over 40,000 m^3/day), especially since commercial RO plants work better under stable conditions [10,11]. Energy storage by batteries has been suggested to overcome RE fluctuations and operate

RO systems at constant load [10,11]. However, their efficiency does not meet the standard needed for use with large-scale applications, as they increase capital cost, add complexity, and require regular replacement [10–12]. This eventually increases water production costs [13,14].

Because of these limitations, the technology of RE-driven RO is either limited to small-scale applications or to large-scale systems that rely on a grid connection to allow for a constant load [11,15–17]. Although a grid-connected RE-driven RO system has lower emissions than a system powered only by fossil fuels, the lack of a load management strategy to meet the fluctuations in RE makes these systems highly dependent on fossil fuels. Hence, a grid-connected system can be considered a transitional technology and not a fully sustainable solution. Operation of large-scale RO systems directly by RE is the final goal for sustainable desalination.

Variable operation would allow direct operation of commercial RO

plants by mature renewables, i.e., wind and solar energy, without the need for energy storage and backup systems [17–19]. Variable operation consists of two techniques, the choice of which depends on the extent of RE variation, i.e.:

- **Variable-speed operation:** The RO plant operates at variable production rate and permeate recovery to adjust its power consumption with respect to available energy [17]. This allows fine adjustment in matching the RO system power consumption to RE fluctuations, but only over a limited power range.
- **Modular operation:** The RO units/trains are connected/disconnected depending on available energy. This relies on the modularity of RO systems to tackle the intermittency and considerable power variations of RE sources [20]. Though it accommodates larger variations, this technique only allows discrete changes in power input.

The possibility of combining variable-speed operation and modular operation as a load management technique for large-scale RO systems would give the greatest flexibility [19]. However, there are technical challenges in implementing variable operation in large-scale application [17]. This paper focuses on tackling operation limitations specific to variable-speed operation.

To operate a RO system at variable speed, two steps are required. Initially, a safe operational window is defined to set the boundaries of acceptable variation in operating parameters [21–23]. Then, an operational strategy is selected that defines the systematic approach for varying the operation parameters with respect to available power, thus matching the RO consumption to available RE.

A study performed by Pohl et al. [23] compared the performance of four operational strategies for a simple RO plant connected to a RE source. The strategies controlled the feed flowrate and feed pressure to operate the system at either constant feed flow, constant feed pressure, constant concentrate flow or constant permeate recovery. The study concluded that maintaining constant permeate recovery provided the optimum performance regarding SEC, permeate quality and range of operation. Although more recent studies [24,25] have used constant recovery, others have used different operational strategies [26–28], suggesting that the optimum operational strategy depends on system design and operation requirements. This emphasizes the importance of using system configurations and components that are used in large-scale systems to develop solutions that are transferable to commercial applications [17].

Another challenge is developing a control system having a fast and robust performance to withstand changes in operating parameters or feed conditions when implementing the chosen operational strategy. Although the control system performance is crucial, only a few studies have discussed this topic for RE-powered RO plants [17,29]. An investigation by Carta et al. [24] reported a mismatch between power generated by a wind turbine and the power consumption of a small-scale RO plant, despite using a stable 2-minute resolution wind speed signal as an input. Advanced control systems were recommended for their fast response in adjusting controlled variables, despite RE fluctuations and RO system inertia [17,24,30,31].

This study aims to improve the efficiency of variable-speed operation of RE powered RO systems to facilitate implementation for large-scale application. The RE source considered is wind energy, as it is a good representation of a fluctuating and intermittent energy source not having a specific pattern. Other types of RE, such as solar, generally vary more slowly and predictably; therefore, a solution developed for wind is expected to accommodate a range of RE types. The objectives for this study are to:

- Present an optimised variable-speed operation technique using a RO system having comparable performance to large-scale plants.

- Investigate and compare the performance of alternative operational strategies for varying the operating parameters according to changes in available power from a wind turbine.
- Design and implement an advanced control system based on Model Predictive Control (MPC) and compare its performance to a conventional Proportional-Integral-Differential (PID) controller.

The paper is structured as follows. Section 2 presents the design of the RO system used. Section 3 describes the development of the RO system dynamic model that is used in control system design and testing. Section 4 outlines the control system design process, including the development of an operational window, identifying the optimum operational strategy, defining the general control system structure, and describing the designs of the PID and MPC controllers. The results and discussion are presented in Section 5, where a summary of the model validation is provided. The effect of feed conditions on system performance is also introduced, and the analysis and implementation of an optimum operational strategy are described. A detailed comparison between the conventional PID controller and MPC is also performed. Section 6 presents an outlook on large-scale implementation of RE-driven RO, followed by Section 7, which summarises the findings and conclusions of this study.

2. RO system description

The RO system, shown in Figs. 1 and 2, is a pilot RO plant designed for testing the operation of RE-driven RO systems. It was designed to have essential features of large-scale systems and thus comparable performance. It includes two parallel pressure vessels, each containing three 8″ RO elements arranged in series. The system is arranged in a split-feed flow configuration, following the current industry practice of splitting the feed between a High-Pressure Pump (HPP) and an Energy Recovery Device (ERD). The plant's rated production capacity is 3.2 m³/ h. A schematic diagram of the system is shown in Fig. 3 and main system specifications are presented in Table 1.

The HPP and ERD were selected from equipment designed for large-scale systems to investigate their ability to operate efficiently with variable power. Positive displacement devices were selected, as they offer consistent efficiency over their operating range. The HPP used is the APP 3.5 axial piston pump manufactured by Danfoss [32]. As for the ERD, isobaric pressure exchangers are favourable for large-scale systems due to their flexibility and modularity, offering high efficiency over the range of operating conditions [17]. The ERD used is the 'Danfoss iSave 21 Plus', which consists of an isobaric pressure exchanger coupled to a vane pump, both driven by the same motor on a single shaft, offering flexibility and precision in controlling flowrate through the ERD [33]. The HPP and ERD motors are powered using Variable Frequency Drives (VFD) to control their speed of rotation and thus flowrate through each device. This allowed control of permeate output and recovery ratio in response to changes in available power, feed concentration and feed temperature.

3. Dynamic modelling of the wind-RO system

This section describes the model developed to predict the dynamic performance of the wind-powered RO system. Initially, the model for the whole RO system is introduced, including RO modules and pumping system, followed by the wind turbine model. The dynamic model was used in the development and testing of the control system, and of the variable operation procedure. It has been implemented in MATLAB-Simulink and validated using experimental data from the laboratory RO system.

3.1. RO system model

The dynamic RO system model uses the solution-diffusion model to
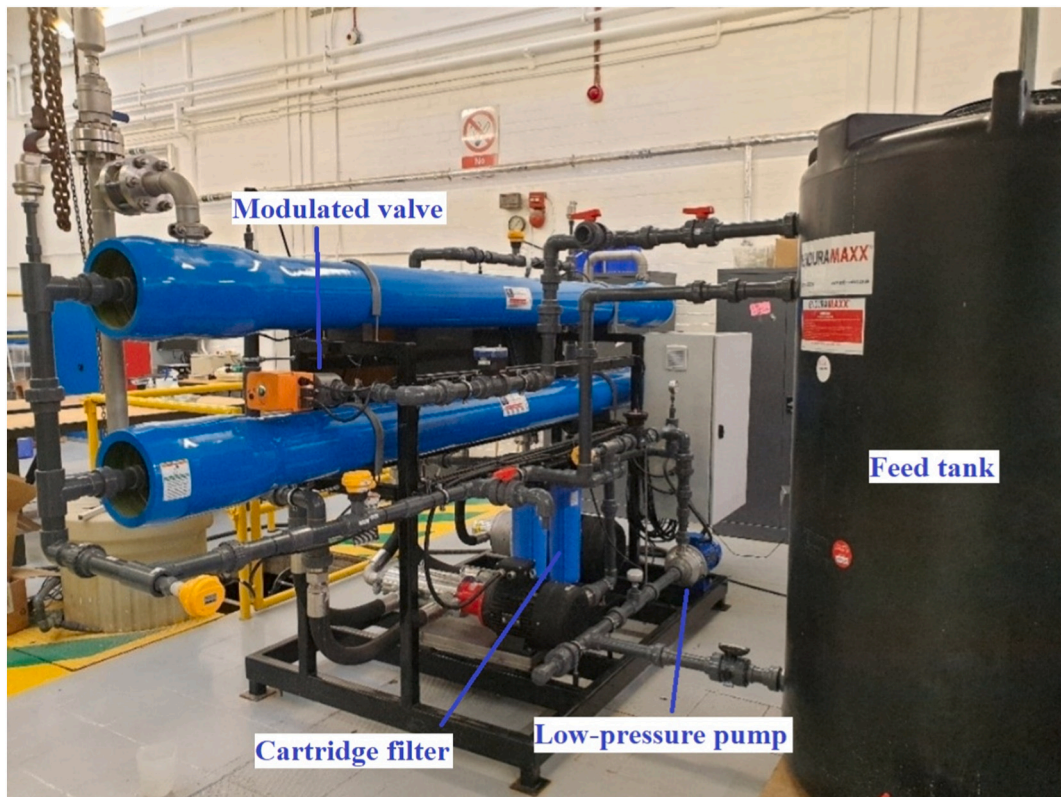
Fig. 1. RO system installed in the laboratory (front).
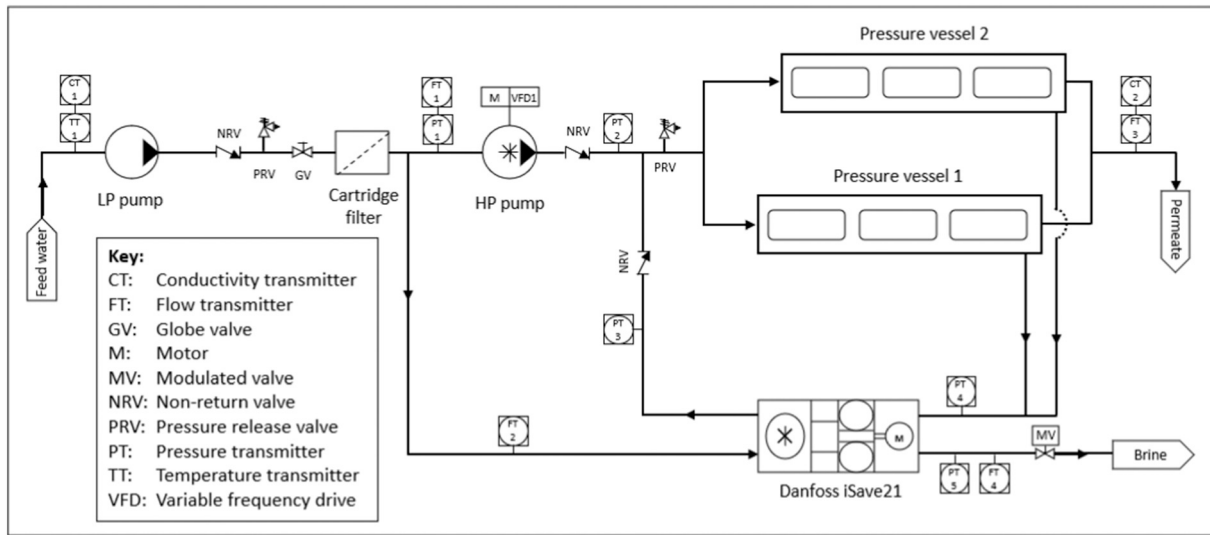

Fig. 2. RO system installed in the laboratory (back).

Fig. 3. Schematic diagram of the laboratory RO system.

Table 1
RO system main specifications.

Membrane type	FilmTec™ SW30HRLE-400
System arrangement	Two pressure vessels in parallel, each containing three RO elements in series
Rated permeate production	3.2 m³/h
Rated permeate recovery ratio	25%
Rated power consumption	7.5 kW
Rated specific energy consumption	2.34 kWh/m³
Feedwater	Salinity 35,000 mg/l Temperature 25 °C
Low-pressure pump	LOWARA CEA210/5/D-V
High-pressure pump	Danfoss APP 3.5
Energy recovery device	Danfoss iSave 21 Plus

describe water and salt transport across the membrane [34]. In addition, concentration polarization is described using the analytical film theory to estimate the mass transfer coefficient variation along the membrane surface within the boundary layer [35]. The RO modules used in this study are the FilmTec™ SW30HRLE-400 8-inch membrane (see specifications in Table 2). The assumptions made throughout this model are as follows:

- The solution-diffusion model is valid.
- The clearances between RO elements inside a pressure vessel are neglected. This allows the in-series RO elements to be modelled as a single element having the same total length and membrane area.
- The pressure in the permeate channel is atmospheric.
- The membrane sheets are modelled as flat channels with negligible curvature.

Table 2
Specifications of the SW30HRLE-400 membranes [36–39].

Parameter	Value
Active area (A_m)	37 m²
Module diameter (d)	0.2 m
Membrane length (l_{bc})	0.8665 m
Membrane width (w_{bc})	1.34 m
Number of membrane leaves/brine channels (n_l)	16
Feed-spacer thickness (t_{sp})	0.7112×10^{-3} m
Brine channel thickness (t_{bc})	0.7112×10^{-3} m
Permeate channel thickness (t_{pc})	0.5×10^{-3} m
Brine channel void fraction (ϕ_{bc})	0.9
Water transport coefficient (A_w)	4.39×10^{-7} m/bar.s
Salt transport coefficient (B_s)	1.35×10^{-8} m/s

- The flow in the spiral direction is assumed negligible.
- The feed, brine and permeate temperatures are equal and constant along the membrane.
- Despite variations in permeate concentration along the permeate channel length, the average value is regarded as the output permeate concentration.
- The feedwater is prepared using a sodium chloride (NaCl) solution to achieve the same osmotic pressure as seawater.
- The brine channel thickness is equal to the feed-spacer thickness ($t_{bc} = t_{sp}$) and the permeate channel thickness, t_{pc}, is assumed 0.5×10^{-3} m [36,37].
- Empirical equations used to calculate the feedwater properties, i.e., density (ρ), viscosity (μ) and brine diffusivity (D_B), are described in Appendix A.

3.1.1. RO modules

The split-feed flow configuration forms two flow loops around the pressure vessels. The outer loop flow, Q_{HPP}, is pressurised by the HPP and represents the permeate portion of the feed stream. The inner loop flow, Q_{iSave}, is pressurised by the iSave and represents the brine portion of the feed stream. A defined quantity of the brine stream (0.5–4%), Q_{Lub}, is used in the iSave to lubricate moving parts [40]. This quantity is lost to system discharge along with the reject brine. The lubrication flow is supplied by the HPP and can be verified experimentally by subtracting the permeate flow, Q_p, from the HPP outlet flow, Q_{HPP} [40]. An empirical relation to calculate the lubrication flow can be found in Fig. B.1 in Appendix B. In the steady-state condition, the flow balance per pressure vessel can be described as follows:

$$Q_f = (Q_{HPP} + Q_{iSave})/N_{pv} \tag{1}$$

$$Q_b = (Q_{iSave} + Q_{Lub})/N_{pv} \tag{2}$$

$$Q_p = (Q_{HPP} - Q_{Lub})/N_{pv} \tag{3}$$

where Q_f is the feed flowrate, Q_b is the brine flowrate and N_{pv} is the number of pressure vessels.

RO relies on applying pressure higher than the osmotic pressure forming a net driving pressure that pushes water through the membrane. This process is described by the solution-diffusion model as follows:

$$J_w = \frac{Q_p}{A_m} = A_w TCF(\Delta P - \Delta \pi) \tag{4}$$

where J_w is the permeate water flux and A_w is the membrane water permeability coefficient. A_m is the membrane active area calculated by:

$$A_m = 2n_e n_l w_{bc} l_{bc} \tag{5}$$

where n_e is the number of RO elements in series, n_l is the number of membrane leaves that are folded to form the feed channel, w_{bc} is the membrane width and l_{bc} is the membrane length. The pressure difference across the membrane, ΔP, is calculated using Eq. (6) as:

$$\Delta P = P_f - P_p - \frac{P_{drop}}{2} \tag{6}$$

where P_f and P_p are the feed and permeate pressures, respectively. P_{drop} is the pressure drop along the membrane that is given by:

$$P_{drop} = 0.01 \frac{1}{14.8} n_e \left(\frac{3600}{0.227} Q_{bulk} \right)^{1.7} \tag{7}$$

where Q_{bulk} is the bulk flowrate inside the brine channel. The osmotic pressure difference across the membrane, $\Delta\pi$, is calculated from Eq. (8) as follows:

$$\Delta\pi = n_i R(T+273) \frac{1}{MW} \left(C_w - C_p \right) \tag{8}$$

where R is the universal gas constant, n_i is the number of moles in a NaCl molecule, MW is the NaCl molecular weight, T is the feedwater temperature in °C, C_w is the average concentration on the membrane wall and C_p is the product water concentration. The coefficients of water permeability, A_w, and salt permeability, B_s, are calculated empirically from the solution-diffusion model using data collected along the operation range at a feed temperature of 25 °C. Variations in water and salt permeability due to changes in feed temperature are accounted for using an empirical temperature correction factor, TCF, provided by the manufacturer as follows [41,42]:

$$TCF = \begin{cases} exp\left[2640 \left(\frac{1}{298} - \frac{1}{273+T} \right) \right]; T \geq 25\text{o}C \\ exp\left[3020 \left(\frac{1}{298} - \frac{1}{273+T} \right) \right]; T \leq 25\text{o}C \end{cases} \tag{9}$$

Feed pressure after the positive displacement HPP is dependent on the system backpressure, which is caused by the osmotic pressure gradient across the membrane. Thus, the feed pressure, P_f, is calculated from a derivation of the permeate flux equation as follows:

$$P_f = \frac{1}{A_w TCF} \frac{(Q_{HPP} - Q_{Lub})/N_{pv}}{A_m} + P_p + \frac{P_{drop}}{2} + \Delta\pi \tag{10}$$

where the brine pressure, P_b, is calculated according to the pressure drop along the brine channel by:

$$P_b = P_f - P_{drop} \tag{11}$$

Based on the concentration polarization theory, the average seawater concentration at the membrane wall, C_w, is calculated as:

$$\frac{C_w - C_p}{C_{bulk} - C_p} = exp\left(\frac{J_w}{K_m} \right) \tag{12}$$

where C_{bulk} is the bulk flow concentration and K_m is the mass transfer coefficient through the membrane, which is calculated using Sherwood analogy as follows:

$$Sh = \frac{K_m d_h}{D_B} = 0.2 Re^{0.57} Sc^{0.4} \tag{13}$$

where Sh is the Sherwood number, d_h is the hydraulic diameter of the brine channel, Sc is the Schmidt number and Re is the Reynolds number in the brine channel [36,43,44]. The Schmidt number is calculated as

follows:

$$Sc = \frac{\mu}{\rho D_B} \tag{14}$$

where μ is the feedwater viscosity and ρ is the feedwater density. As for the Reynolds number inside the brine channel, it is given by:

$$Re = \frac{\rho d_h V_{bulk}}{\mu} \tag{15}$$

where V_{bulk}, the bulk flow velocity through the brine channel, is calculated as follows:

$$V_{bulk} = \frac{Q_{bulk}}{n_l w_{bc} t_{bc} \phi_{bc}} \tag{16}$$

where t_{bc} is the brine channel thickness and ϕ_{bc} is the void fraction that represents the reduction of void volume inside the brine channel [36,45]. The hydraulic diameter, d_h, represents the non-circular geometry of the spacer-filled brine channels. It is calculated using the void fraction, ϕ_{bc}, and the feed spacer thickness, t_{sp}, to include the effect of the spacer's surface area on the flow as follows [36,45]:

$$d_h = \frac{4\phi_{bc}}{\frac{2}{t_{sp}} + (1 - \phi_{bc})\frac{8}{t_{sp}}} \tag{17}$$

As a result of high concentration difference between the brine and product water streams, salt permeates the membrane along with water molecules. This mass transport phenomenon can be described by Eq. (18), which represents the salt transport flux J_s as follows:

$$J_s = B_s TCF exp\left(\frac{J_w}{K_m} \right) \left(C_{bulk} - C_p \right) \tag{18}$$

The transient characteristics of the RO module performance are associated with variation in brine concentration along the membrane length. These variations directly affect the system pressure response and permeate flowrate through changes in osmotic resistance. The change in bulk flow concentration, C_{bulk}, related to salt accumulation in the membrane channel, is represented by the salt balance along the membrane length and through the active layer using the concentration conservation formula as follows:

$$V_{bc} \frac{dC_{bulk}}{dt} = Q_f C_f - Q_b C_b - Q_p C_p \tag{19}$$

where the brine channel volume, V_{bc}, and the brine concentration, C_b, are calculated respectively from Eqs. (20) and (21) as:

$$V_{bc} = n_e n_l w_{bc} l_{bc} t_{bc} \phi_{bc} \tag{20}$$

$$C_b = 2C_{bulk} - C_f \tag{21}$$

Similarly, the transient change in the bulk permeate flow concentration, C_p, is given by:

$$V_{pc} \frac{dC_p}{dt} = Q_p C_{p,m} - Q_p C_p \tag{22}$$

where $C_{p,m}$ is the local permeate concentration at the membrane surface and V_{pc} is the permeate channel volume, which are given respectively by Eqs. (23) and (24) as follows:

$$C_{p,m} = \left(\frac{J_s}{J_w} \right) \tag{23}$$

$$V_{pc} = n_e n_l w_{bc} l_{bc} t_{pc} \phi_{pc} \tag{24}$$

Although the above equations describe the output streams characteristics for a single pressure vessel, they can also be used to predict the same outputs for a RO unit containing multiple pressure vessels. Thus, the permeate flowrate, permeate concentration, brine flowrate and

brine concentration from the two pressure vessels ($N_{pv} = 2$) are calculated, respectively, as follows:

$$Q_p = \sum_{i=1}^{N_{pv}} Q_{p,i} \tag{25}$$

$$C_p = \frac{\sum_{i=1}^{N_{pv}} C_{p,i} Q_{p,i}}{Q_p} \tag{26}$$

$$Q_b = \sum_{i=1}^{N_{pv}} Q_{b,i} \tag{27}$$

$$C_b = \frac{\sum_{i=1}^{N_{pv}} C_{b,i} Q_{b,i}}{Q_b} \tag{28}$$

3.1.2. Pumping system

The detailed model for the Low-Pressure Pump (LPP), HPP and iSave are presented in Sections B.1, B.2, and B.3 in Appendix B, respectively. Each section outlines the flowrate and power consumption calculation of the respective unit. The total power consumption of the RO system is thus calculated as follows:

$$P_{e,total} = P_{e,LPP} + P_{e,iSave} + P_{e,HPP} \tag{29}$$

3.2. Wind turbine

The wind turbine used in the simulations is the Ryse Energy E-10, which is a 3-bladed horizontal axis wind turbine that delivers 10 kW rated power, thus matching the power requirement of the laboratory RO system [46]. Initially, the wind turbine performance was represented using a single-mass dynamic model, as in [47], which included the rotor and generator inertia in the rotor speed calculation. However, the inertial response was found to be negligible due to the low mass of the rotor and generator assembly, which showed an insignificant delay in rotor speed relative to changes in wind speed. The effect of such inertia would be more significant for larger wind turbines and would tend to smooth the power output under fluctuating wind conditions. Thus, for the selected turbine, a quasi-steady-state model was used to calculate the wind power using the wind turbine power curve. This quasi-steady-state model reflects the real-time wind speed fluctuations without any delays, leading to the design of a more robust control system. If the control system can accommodate the rapid fluctuations from a small, zero-inertia wind turbine, it will also be able to accommodate those from a larger turbine, and from a range of RE sources in general. The wind turbine power curve for the E-10 wind turbine is presented in Fig. 4 [46].
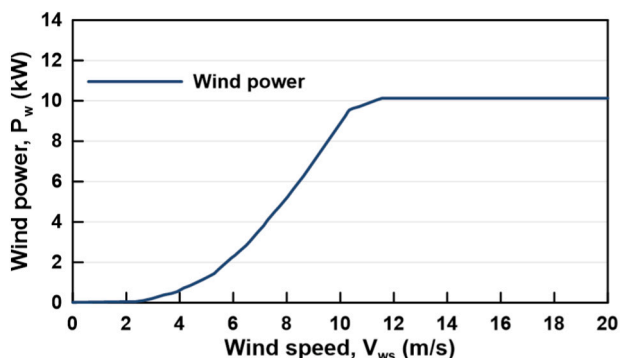

Fig. 4. Wind turbine power curve.

4. Control system design

Variable-speed operation involves operating the RO system as a variable load by controlling the parameters directly affecting its power consumption [17]. This requires a control system that delivers fast and robust performance while operating within the boundaries of safe operation, to avoid exceeding the hydraulic limitations of the components and to guarantee an acceptable permeate quality. This section describes the control system design process. Initially, a safe operational window and an operational strategy for varying the operating parameters are developed. The general structure of the control system is defined based on the process design and control objectives. The designs of the PID and MPC controllers are also presented.

4.1. Operational window

The operational window defines the acceptable range of parameter variation for safely operating the RO system. Several studies [21–23] have presented design specific operational windows but all using the same general concept. The window is defined based on the RO membrane constraints across the feed pressure and flowrate using the Reverse Osmosis System Analysis (ROSA) software. A full description of the procedure can be found in [23]. Constraints of the FilmTec™ SW30HRLE-400 membranes are described as follows [23,41]:

1) Maximum feed pressure that the membrane can withstand (83 bar).
2) Maximum allowed feed flow based on the membrane mechanical loading (14 m^3/h).
3) Maximum permeate flow per element (1.4 m^3/h) and the maximum recovery per element (13%) that could lead to excessive concentration polarization.
4) Minimum concentrate flow to avoid salt precipitation and membrane fouling (3.4 m^3/h).
5) Maximum product concentration based on the recommendations of the World Health Organisation (500 mg/l).

As presented in Fig. 5, the operational window was defined for two pressure vessels in parallel, each containing three SW30HRLE-400 RO elements in series, for feedwater of 35,000 mg/l NaCl concentration at 25 °C. During the process of RO system development, the system design and component selection reflected the limitation imposed by the operational window.

4.2. Operational strategy

The operational strategy defines the approach to varying the plant operating parameters according to changes in wind power [17]. The optimum strategy should permit a wide operation range, allowing for longer periods of permeate production, and operating at the lowest SEC, to efficiently utilise the available power [48]. An investigation was performed to determine the optimum operational strategy considering, a) operation at constant recovery, b) operation at constant brine flowrate and c) operation at a constant feed flow. Operation at constant feed pressure was not considered, as it requires maintaining a constant permeate flowrate, thus not serving the purpose of variable production [23]. The operating parameters were then mapped corresponding to the RO system power consumption and embedded into the control system. The results are presented in Section 5.3.

4.3. General control structure

Determining the control system structure is the first step in process control design. It includes identifying the manipulated, disturbance, and controlled variables that directly affect system performance. The manipulated variables are input parameters that are varied by the control system, e.g., pump speed or valve opening, to maintain the
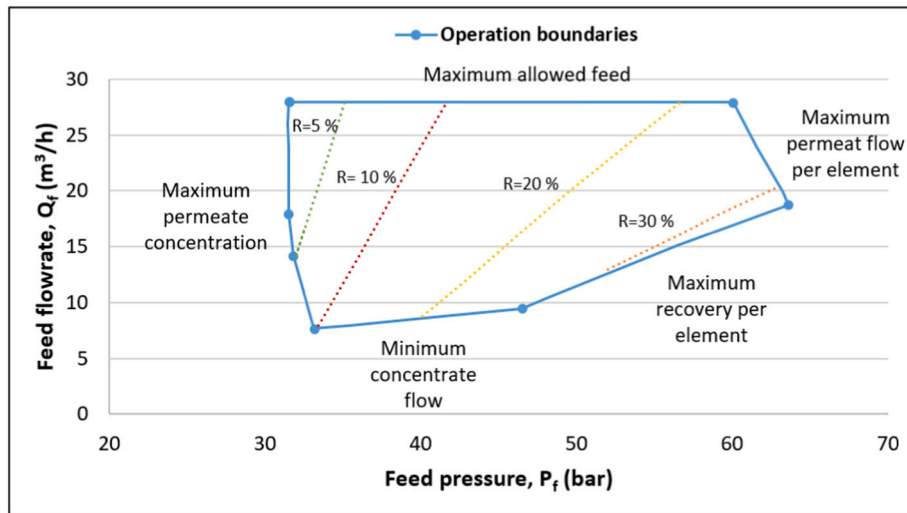
Fig. 5. Safe operational window.

controlled outputs, e.g., flowrate or pressure, at a reference value. For RO systems, the manipulated variables and controlled outputs directly affecting the power consumption depend on system design and used equipment. Previous studies [21,23,24] have used feed flowrate and feed pressure as controlled outputs for varying the power consumption. This concept is true for systems using a throttle valve, a Pelton wheel, or a turbocharger on the brine reject line. These can offer active control of the feed pressure by manipulating the throttle valve opening or changing the input nozzle valve opening in case of a Pelton turbine or a turbocharger [17]. However, for the system used in this study and for systems using split-feed flow configuration in general, their operational control is based purely on flow control, such that the variation in system pressure is a by-product of changes in permeate flowrate, brine flowrate, feed concentration and temperature. This in turn creates two independent control loops, by which the HPP speed, N_{HPP}, directly controls the permeate flowrate and the iSave speed, N_{iSave}, directly controls the brine flowrate, and both ultimately dictate the power consumption. Accordingly, the control system manipulated variables are the HPP speed, N_{HPP}, and iSave speed, N_{iSave}, while the controlled outputs are the permeate flowrate, Q_p, and brine flowrate, Q_b. The input disturbances are the feed conditions, i.e., feed concentration, C_f, and feed temperature, T_f.

Fig. 6 presents the finalised control system structure to be used for the PID and MPC controllers. The control system generates the control signal based on available wind power and input disturbances. The control system consists of the embedded operational strategy, described

in Section 5.4, which generates the set-points for the permeate and brine flowrates corresponding to specific power consumption, in addition to the controller that generates the control signal for the manipulated variables depending on the error value.

4.4. Proportional-integral-differential control

PID control is the most widely used process control technique for industrial applications, due to its simplicity and effectiveness [49]. The transfer function of a standard PID controller is presented in parallel form as follows:

$$G(s) = K_p + K_i \frac{1}{s} + K_d s \tag{30}$$

where K_p is the proportional gain, K_i is the integral gain, K_d is the differential gain [50]. The proportional gain delivers a control action proportional to the present error value between plant input and the reference signal. The integral term eliminates steady-state error by summing the error over time. The derivative term adds damping and decreases overshoot by generating a control signal proportional to the rate of change of the process variable. For this study, only the proportional and integral terms were used, since the RO system open-loop response exhibited minimal overshoot and to avoid system instability that could occur due to sensor noise [24]. The derivative term was set to zero.
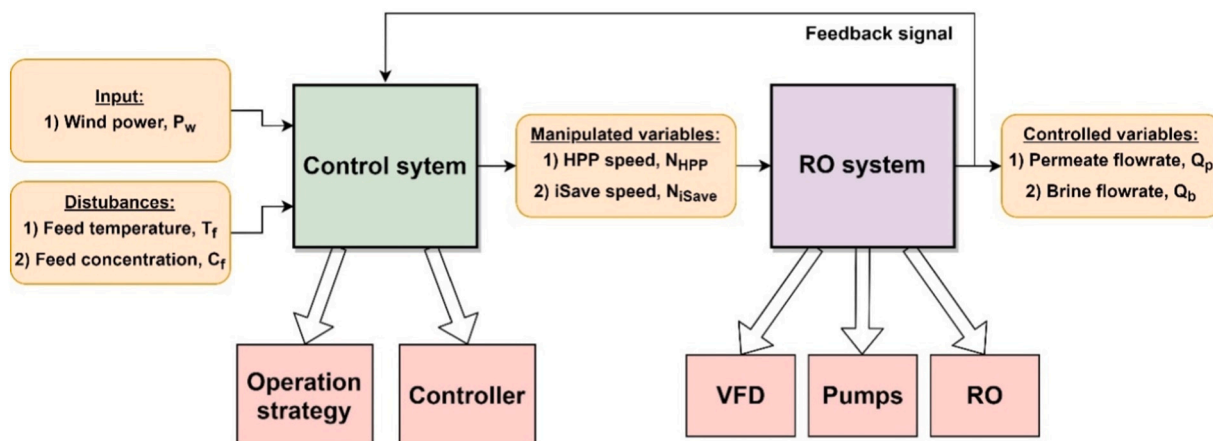

Fig. 6. High-level block diagram showing the control system structure and signals between each element.

The PID controller performance is dependent on the proportional, integral, and derivative gains. These tuning parameters are selected to generate a desired response based on the process dynamics [51]. The PID tuning parameters were initially selected using the open loop Ziegler-Nichols tuning method, a popular PID tuning technique, and were later adjusted using the MATLAB PID Tuner to obtain an optimised performance [51,52]. The PID Tuner allows for tuning the controller gains based on response time and transient behaviour for a step-input in the time domain [53–55]. The tuning parameters were selected to deliver the fastest rise time with minimum overshoot, while maintaining a change in pump speeds below 2 Hz/s for smooth operation [56]. The finalised PID tuning parameters are presented in Table 3. A schematic diagram of the PID controller developed is presented in Fig. 7. Depending on the wind turbine power and the selected operation strategy, the PID controllers receive reference signals for the permeate flowrate, $Q_{p,ref}$, and the brine flowrate, $Q_{b,ref}$, The controllers then generate control signals for the HPP speed, N_{HPP}, and iSave speed, N_{iSave}, which are sent to the VFDs for generating a variable frequency electric signal for the HPP, F_{HPP}, and iSave, F_{iSave}. The relation between the pump speeds, N, and input frequencies, F, are presented in Appendix B, Sections B.2 and B.3 for the HPP and iSave, respectively.

4.5. Model predictive control

MPC is an advanced control technique that is becoming increasingly popular for process control [57]. Unlike traditional PID control, MPC is specifically designed for multiple-input multiple-output systems and can handle system constraints such as those occurring in the RO process [49,58].

As shown in Fig. 8, the MPC controller consists of two components: a) a built-in dynamic model that predicts system response towards a control sequence, and b) an optimiser that calculates an optimal control sequence for minimizing the error between output and target values. During operation, the prediction and optimisation procedures are performed in parallel at each sample time, such that a control sequence is calculated from the optimisation problem and then tested on the prediction model for a specific prediction horizon [49]. The controller generates a control signal in the form of HPP speed, N_{HPP}, and iSave speed, N_{iSave}, according to a reference signal for the permeate flowrate, $Q_{p,ref}$, and brine flowrate, $Q_{b,ref}$, and the plant measured outputs.

The MPC algorithm used is a direct extension of the Dynamic Matrix Control, which is a widely used MPC control algorithm [49,59]. It employs a discrete state-space model as the prediction model and a quadratic criterion as the optimiser [60,61]. The MPC controller was developed using the MPC Designer of MATLAB-Simulink. The formulas for the prediction model and optimiser are described as follows:

4.5.1. Prediction model

The discrete linear time-invariant model used for prediction uses the following general form:

$$\boldsymbol{x}(k+1) = A\boldsymbol{x}(k) + B\boldsymbol{u}(k) \tag{31}$$

$$\boldsymbol{y}(k) = C\boldsymbol{x}(k) + D\boldsymbol{u}(k) \tag{32}$$

where k is the sampling time, A, B, C and D are coefficient matrices for the model states, model inputs, model outputs and feedforward matrix, respectively. $\boldsymbol{x}(k)$, $\boldsymbol{u}(k)$ and $\boldsymbol{y}(k)$ are vectors representing the model states, model inputs and model outputs, respectively [62,63]. The state-

space prediction model was generated from input/output data using a data-driven modelling technique called System Identification [64]. System Identification is based on estimating values of the coefficient matrices by minimizing the error between model output and measured response to fit the model to the input/output data [62]. The generated multi-input multi-output state-space model is as follows:

$$\begin{bmatrix} x_1(k+1) \\ x_2(k+1) \end{bmatrix} = \begin{bmatrix} -0.272 & 0 \\ 0 & -17.27 \end{bmatrix} \begin{bmatrix} x_1(k) \\ x_2(k) \end{bmatrix} + \begin{bmatrix} -0.3591 & 0 \\ 0 & 129900 \end{bmatrix} \begin{bmatrix} F_{HPP}(k) \\ F_{iSave}(k) \end{bmatrix} \tag{33}$$

$$\begin{bmatrix} Q_p(k) \\ Q_b(k) \end{bmatrix} = \begin{bmatrix} -0.0507 & 0 \\ 0 & 6.712 \times 10^{-5} \end{bmatrix} \begin{bmatrix} x_1(k) \\ x_2(k) \end{bmatrix} + \begin{bmatrix} 0 & 0 \\ 0 & 0 \end{bmatrix} \begin{bmatrix} F_{HPP}(k) \\ F_{iSave}(k) \end{bmatrix} \tag{34}$$

where the model inputs are the HPP input frequency F_{HPP} and the iSave input frequency F_{iSave}. The model outputs are the permeate flowrate Q_p and the brine flowrate Q_b. The data used for parameters estimation are time-domain input/output data recorded experimentally at 0.1 s sampling interval during an open-loop step-response test of 10% deviation in the pumps' speed from the rated operating point. The model prediction accuracy is represented by its fit to the estimation data and Root Mean Square Error (RMSE) in Table 4.

4.5.2. Optimiser

The MPC uses the prediction model to estimate the controlled outputs $\boldsymbol{y}$ with respect to the manipulated inputs $\boldsymbol{u}$. The error between the predicted output and the reference values is minimised by generating an optimised control sequence $\boldsymbol{u}_k$, $\boldsymbol{u}_{k+1}$, … $\boldsymbol{u}_{k+m-1}$ along the control horizon. The first element of the control sequence $\Delta\boldsymbol{u}(k)$ is sent to the plant as a control signal in the form of $\boldsymbol{u}(k) = \boldsymbol{u}(k-1) + \Delta\boldsymbol{u}(k)$. The remaining samples $\Delta\boldsymbol{u}(k+i)$ are discarded and a new optimisation problem is solved at the next sampling step $k+1$ based on new measurements. This is referred to as the receding horizon approach [65]. The recalculation at each sample time is essential to overcome inaccuracies in prediction and optimisation stages, and periodically make up for any unexpected disturbances. The control action at time k is calculated by solving the optimisation problem as follows [62,63]:

$$\min_{\Delta\boldsymbol{u}(k),...,\Delta\boldsymbol{u}(k+H_c-1)} \boldsymbol{J} = \sum_{i=0}^{H_P-1} \boldsymbol{W}_y \Big[\boldsymbol{y}(k+i+1) - \boldsymbol{y}(k+i+1)_{ref} \Big]^2$$
$$+ \sum_{i=0}^{H_c-1} \boldsymbol{W}_{\Delta u} [\Delta\boldsymbol{u}(k+i)]^2 + \sum_{i=0}^{H_c-1} \boldsymbol{W}_u \Big[\boldsymbol{u}(k+i) - \boldsymbol{u}(k+i)_{ref} \Big]^2$$

$$\text{Subject to:} \begin{cases} \boldsymbol{y}_{min} < \boldsymbol{y}(k+i) \langle \boldsymbol{y}_{max} \\ \Delta\boldsymbol{u}_{min} < \Delta\boldsymbol{u}(k+i) \langle \Delta\boldsymbol{u}_{max} \quad \text{, For } i = 0, ..., H_P-1 \\ \boldsymbol{u}_{min} < \boldsymbol{u}(k+i) \langle \boldsymbol{u}_{max} \end{cases} \tag{35}$$

where $\boldsymbol{W}_u$ and $\boldsymbol{W}_{\Delta u}$ and $\boldsymbol{W}_y$ are the inputs, inputs increment and outputs weight factors, H_p and H_c are the prediction and control horizon, respectively. The weights set the priority of each variable behaviour to the overall performance. The prediction horizon, H_p, is the future time horizon before which the controller aims to achieve the desired output response. It was selected to cover the process steady-state response to ensure that the entire process dynamics are considered and anticipate constraints violation early enough to allow for corrective action [66]. The control horizon, H_c, is the number of time steps of the control sequence that is computed. It was selected at a small value that would reduce the required computations while providing a robust control action [63]. The calculation of the control sequence using the objective function is subject to a set of constraints that are specific to the plant's input/output physical limitations. The control parameters, constraints and weights defined for the MPC controller are presented in Table 5.

Table 3
Proportional-Integral-Differential (PID) tuning parameters. Derivative gain is set to zero for both controllers.

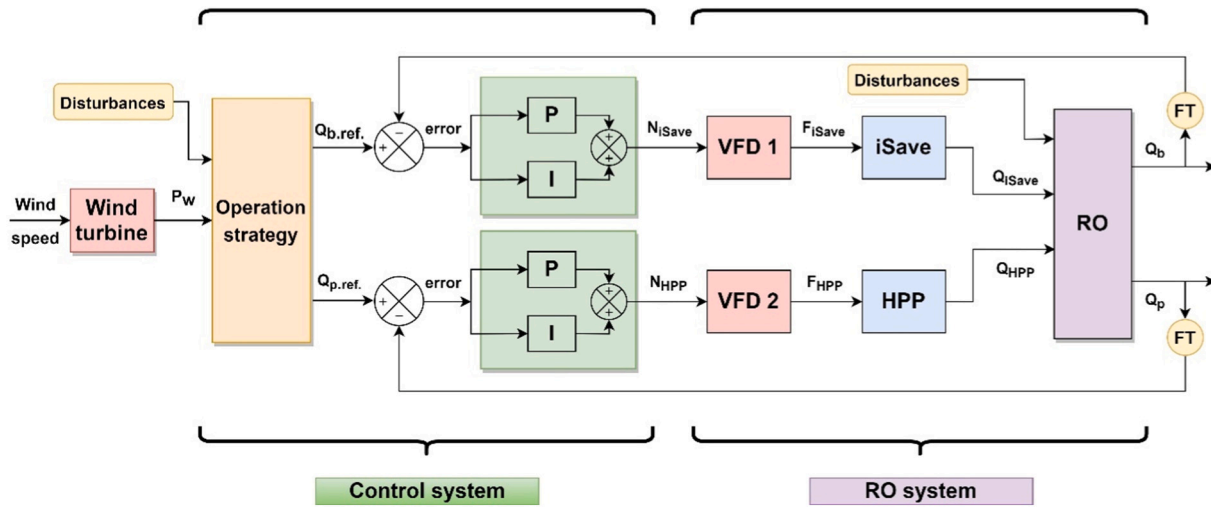|	Proportional gain (K_p)	Integral gain (K_i)
High-pressure pump	1.607	4.02
Danfoss iSave	0.1	0.615

Fig. 7. Structure of the Proportional-Integral-Differential controller. FT represents the flow transmitters sending feedback signals to the controller.
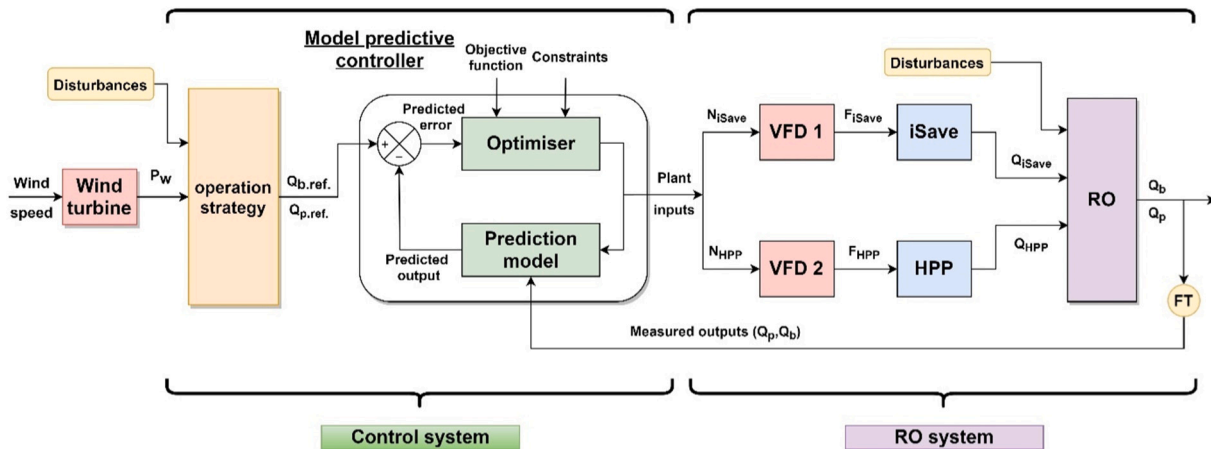

Fig. 8. Structure of the model predictive controller.

Table 4
Prediction accuracy of the State-Space model compared to the estimation data.

	Fit to estimation data	RMSE
Permeate flowrate, Q_p	86.83%	0.00212
Brine flowrate, Q_b	81.25%	0.00581

5. Results and discussion

5.1. Model validation

The developed model was validated for predicting steady-state outputs and dynamic responses using experimental data collected from the lab RO system for defined inputs, i.e., the HPP and iSave speeds, and input disturbances, i.e., feed temperature and concentration.

For the steady-state validation, the model showed high accuracy for predicting the permeate flowrate, feed pressure and power consumption presented by a coefficient of determination (R^2) of 0.93, 0.98 and 0.99, respectively. The prediction accuracy for the permeate concentration was more modest compared to other parameters, at an R^2 of 0.77, due to an overestimation of the permeate concentration at low flowrates. To ensure that this overestimation is not a modelling error, the simulated data were compared to that of ROSA, at the same inputs and disturbances, and an accuracy presented by an R^2 of 0.97 was achieved for the

Table 5
Summary of the Model Predictive Controller tuning parameters.

Controller parameter	Value
Sample time (k)	0.1 s
Prediction horizon (H_p)	50 samples
Control horizon (H_c)	2 samples

Input constraints	Range	Rate
iSave speed (F_{iSave})	0–50 Hz	2 Hz/s
HPP speed (F_{HPP})	0–50 Hz	0.5–2 Hz/s

Output constraints	Range	Weight (W_y)
Permeate flowrate (Q_p)	0–3.5 m³/h	1
Brine flowrate (Q_b)	0–18 m³/h	1

permeate concentration, which validated the model accuracy. The experimental and simulated steady-state validation data are included in Supplementary material 1, Appendix C.

As for the dynamic response, the predicted and measured data remained within a 5% error margin when predicting transient changes in permeate flowrate, feed pressure, and permeate concentration for a

10% step-change in the HPP rotational speed, N_{HPP}. Overall, the model was found to be reliable for predicting the steady-state and dynamic performance and is sufficient to support the conclusions reached. Details on the validation procedure and discussion on the model accuracy are included in Supplementary material 2, Appendix C.

5.2. Effect of feed conditions on performance

The feed conditions of a RO system, i.e., feed concentration and temperature, can affect its performance by altering the power consumption for the same HPP and iSave speeds. This is particularly evident for RO systems subject to seasonal variations in feed water temperature and tidal variations in feed concentration. Thus, an important step in control system design is to analyse their effect as an input disturbance on the RO plant operation. This is beneficial for examining the controller's ability to maintain a target value despite changes in input feed conditions.

5.2.1. Feed concentration

Fig. 9 presents the effect of feed concentration on operating parameters. The feed concentration was varied from 25,000 to 40,000 mg/l with 5000 mg/l increments. The data were collected experimentally from the RO system at a standard feed temperature of 25 °C with a ± 1 °C uncertainty. Fig. 9 (a) shows that the feed concentration has an impact on the process pressure, such that the feed pressure required to achieve the same permeate flux increased at higher feed concentration. The increase in required pressure led to more torque acting on the HPP motor shaft, thus requiring more power and higher SEC for the same

permeate flux, which is evident in Fig. 9 (b). As for the permeate quality, Fig. 9 (c) shows that the permeate concentration increased for higher feed concentration due to higher salt gradient across the membrane.

5.2.2. Feed temperature

The effect of feed temperature on feed pressure and permeate concentration is presented in Fig. 10. The feed temperature was varied from 20 °C to 30 °C, while the feed concentration was maintained constant at 35,000 mg/l. The reason for including the temperature as an input disturbance is the effect it has on the water and salt permeability of the polymeric membrane. Higher feed temperatures can lead to changes in the physical properties of the membrane structure and possibly, changes in water diffusivity [67]. This was evident from the relationship between permeate flux and feed pressure presented in Fig. 10 (a), which showed that, for the same permeate flux, the required feed pressure was reduced at higher temperatures. As for the permeate quality, Fig. 10 (b) shows an increased permeate concentration for the same permeate flux at higher feed temperature.

5.3. Comparing operational strategies

The operational strategies investigated were operation at constant recovery, constant brine flowrate or constant feed flowrate. A comparison between the operational strategies is presented in Fig. 11. Operation at a constant recovery was considered at three recovery ratios (15, 20, and 24%). For operation at constant brine flowrate, the brine flow was maintained at the minimum flowrate, 9.8 m^3/h, which allows for pressure higher than 1 bar at the iSave brine discharge [33]. The
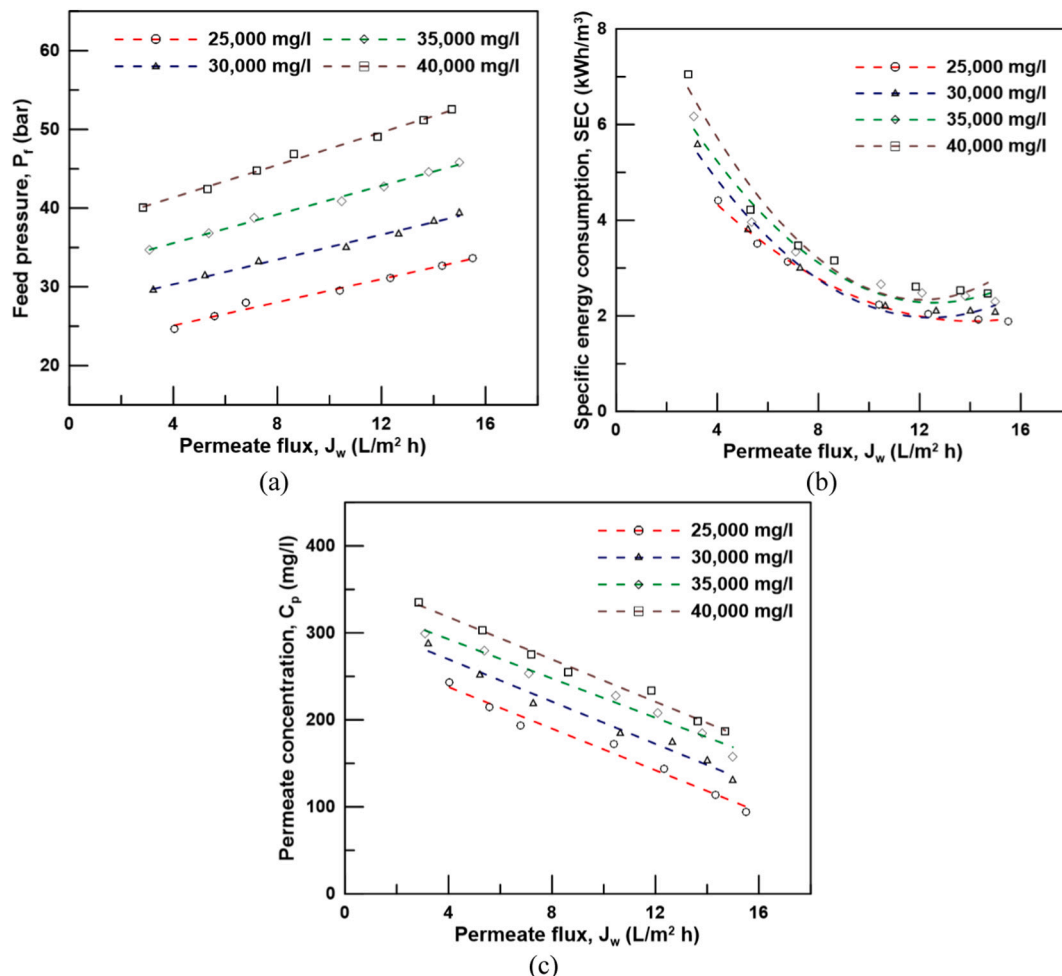

Fig. 9. The effect of feed concentration on a) feed pressure, b) specific energy consumption, and c) permeate concentration.
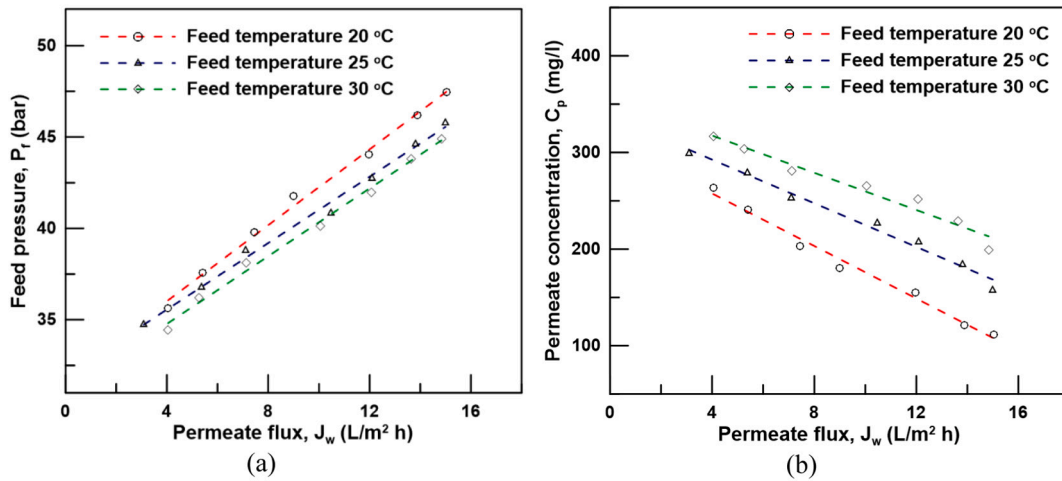
Fig. 10. The effect of feed temperature on a) feed pressure, and b) permeate concentration.
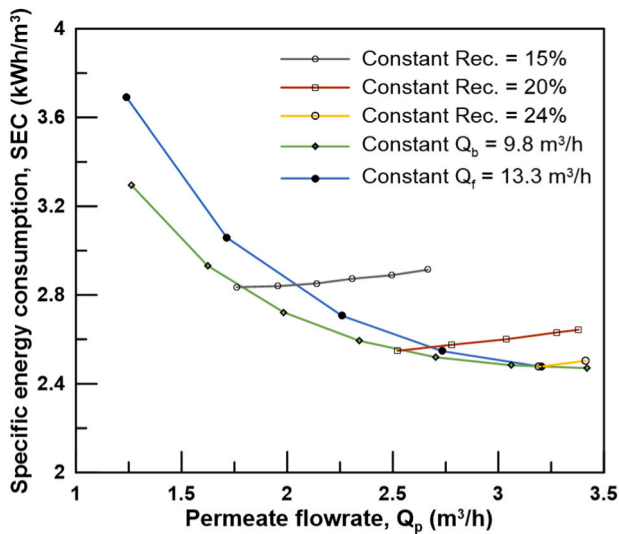

Fig. 11. Comparison of possible operational strategies.

Fig. 12. The developed operational strategy based on variable recovery at a constant brine flowrate.

permeate flowrate was varied independently by manipulating the HPP speed as the brine was maintained constant, achieving variable recovery. For operation using constant feed flow, the permeate and brine flowrates were interchanged to maintain a constant feed flow at 13.3 m³/h, which is the sum of the minimum brine flowrate and maximum permeate flowrate.

In terms of operation range, Fig. 11 shows that operation at variable permeate recovery, i.e., constant brine flow and constant feed flow, guaranteed a wider operation range compared to operation at constant recovery. Moreover, the operation range for operating at constant recovery decreased for higher recovery ratios due to a drop in the brine flowrate below the set minimum.

As for the SEC, operating at constant recovery showed higher SEC compared to other strategies due to higher power consumption by the iSave. For operation at variable recovery, the constant brine flowrate strategy achieved the lowest SEC due to minimised brine flowrate and operation at higher recovery ratios. Accordingly, operation with variable permeate recovery and constant brine flowrate was the optimum operational strategy for this system configuration, as it allowed the widest operation range at the lowest SEC. This finding contrasts with other studies that used constant recovery [23–25], thus highlighting the advantage of using a test rig with similar performance to large-scale systems to determine an operational strategy better suited to such scale.
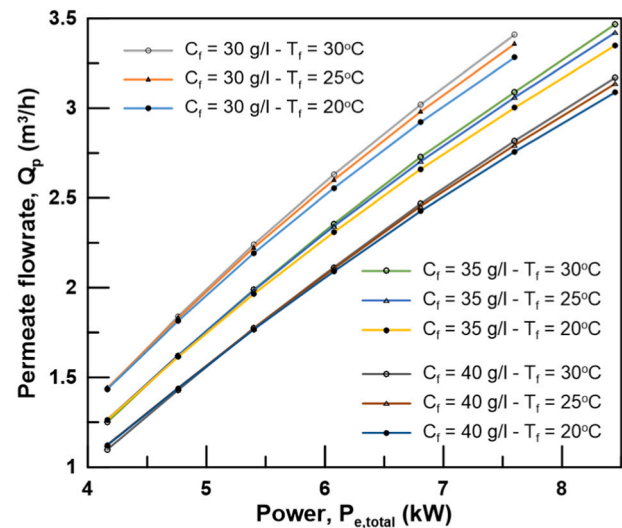
5.4. Implementing the operational strategy

After defining an optimum operational strategy, the controlled parameters were mapped with respect to power consumption, presented in Fig. 12, for the entire operating range while considering input disturbances, i.e., feed temperature and concentration, and maintaining the brine flowrate at a constant value. The data were calculated from the model at feed concentrations ranging from 30,000 to 40,000 mg/l and temperatures ranging from 20 to 30 °C. The fine variation between the concentration and temperature ranges were accounted for by using linear interpolation. The generated operation parameters were embedded into the operational strategy block, described in Section 4.3, and then fed to the controller to generate the control signal for the HPP and iSave depending on the error signal. This approach of selecting the process parameters based on a complete overview of the process inputs (i.e., available power, feed concentration and feed temperature) ensures a match between the RO system energy consumption and available power.

5.5. Comparison of the PID and MPC performance

The performance of the PID and MPC controllers were assessed based on three criteria: a) tracking a reference signal during a step-change in a

controlled variable, b) maintaining a reference signal during a step-change in feed conditions, and c) improvement in permeate production for multiple wind scenarios. The control system analysis was performed using the dynamic model of Section 3.

5.5.1. Tracking a reference signal

The controller's ability to track a reference signal was assessed using a step-response test, whereby the simulation was stabilized and a step input of 10% increase in the controlled output was introduced. The step-response test for the PID controlling the HPP and the MPC was performed by introducing a step-change in the permeate flowrate reference signal from 2.57 m³/h to 2.827 m³/h at a feed concentration of 35,000 mg/l and 25 °C feed temperature. The results, presented in Fig. 13 (a), showed a significant advantage for the MPC controller over the PID. The settling time, time until the error between the actual output and the reference signal is within 2%, for the permeate flowrate improved by 47% from 11.95 s to 6.33 s.

The step-response test performed for the MPC and PID controlling the iSave is presented in Fig. 14. A 10% step-change in the brine flowrate reference signal was introduced from 10.06 m³/h to 11.06 m³/h at a feed concentration of 35,000 mg/l and 25 °C feed temperature. The MPC presented a faster response than the PID controller, improving the settling time by 92.1% from 13.18 s to 1.04 s.

5.5.2. Rejecting disturbances in feed conditions

The ability of the control system to maintain the power consumption at a reference value despite disturbances in feed conditions is examined in this section. Based on the analysis described in Section 5.2, both input disturbances, i.e., feed concentration and feed temperature, influence the system pressure leading to a deviation in power consumption relative to available power, if corrective action is not taken. The disturbance rejection tests were performed for both controllers by introducing a 10% step change in feed concentration from 35,000 to 38,500 mg/l at 25 °C and a 10% step change in feed temperature from 25 °C to 27.5 °C at 35,000 mg/l. The controllers were compared for their ability to maintain a power consumption corresponding to a wind speed of 7.5 m/s against changes in feed conditions.

Fig. 15 shows that the MPC controller offered a faster response to changing the permeate flowrate in response to the step change in feed concetration, such that the settling time improved by 47.2% from 13.3 s for the PID to 7.02 s for the MPC. However, the value of the power consumption reached steady-state at a similar time for both controllers.

Fig. 16 shows the disturbance rejection test for a step-change in feed temperature. An increase in feed temperature led to an increase in membrane permeability, thus decreasing the required power for the same permeate flux. This allowed increasing the permeate flowrate and

maintaining the power consumption at the reference value, thus achieving higher energy utilisation. The MPC showed a faster response to changes in feed temperature, such that the settling time for the permeate flowrate improved by 43.9% from 15.5 s using the PID to 8.7 s using the MPC. As for the power consumption, presented in Fig. 16 (b), the settling time improved from 25.74 s using the PID to 19.36 s using the MPC.

5.5.3. Improvement in permeate production for multiple wind scenarios

The control systems performance was compared during hourly operation by, a) analysing the match between actual and reference permeate production, and b) comparing the permeate production for the same input signal. Three wind speed scenarios with distinct wind speed variations were used, as presented in Table 6. These scenarios were based on a random signal with Gaussian distribution about a mean wind speed of 6.5 m/s. A high-resolution sample time of 10s was selected for the three scenarios to reflect the wind speed fluctuations. The difference in variation intensity between each signal was subject to a standard deviation representing an increasing percentage of the mean speed as shown in Table 6. In addition, a high variation in feed concentration and temperature were introduced for each scenario to include the disturbance rejection performance of both controllers in the assessment. Each scenario was tested for 1 h of operation with the same disturbance signal. A sample of the wind speed time-series used in the medium wind-variation scenario is presented in Fig. 17.

Initially, the ability of the controllers to track a reference signal subject to wind speed fluctuations was assessed. The operational strategy defined in Section 5.4 was used to generate the permeate flowrate reference signal based on available wind power from each scenario. Figs. 18 and 19 show a sample (15 min) of the performance projection for the medium wind-variation scenario compared to the reference signal generated by the operational strategy for the PID and MPC controllers, respectively.

The PID controller showed adequate performance for tracking the reference signal at low wind speed fluctuations. However, there was an evident mismatch between the actual and reference permeate flowrate in cases of high amplitude wind speed variation, highlighted by the dotted circles in Fig. 18, which occurred as a delay in tracking the reference signal or overshoot from the steady-state value. On the other hand, the MPC performance, presented in Fig. 19, showed an efficient match between the actual and reference permeate flowrate at different levels of wind speed variation. The MPC showed less delay in tracking the reference signal and minimal overshoot from the steady-state value. The improved performance delivered by the MPC is associated with its predictive ability to test and optimize the control sequence before execution. A similar improvement occurred in the low and high wind-
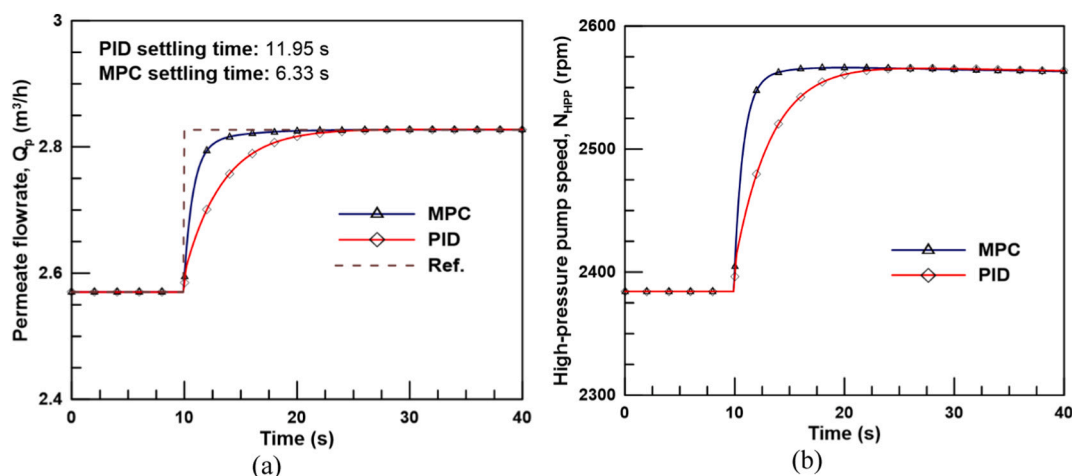

Fig. 13. The simulated PID and MPC controller's response to a 10% step change in the permeate flowrate reference signal.
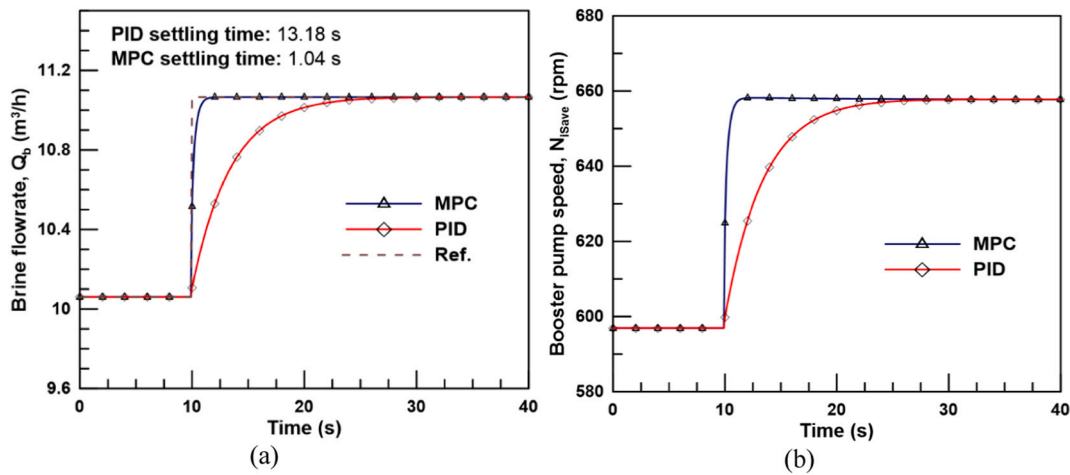
Fig. 14. The simulated PID and MPC controller's response to a 10% step change in the brine flowrate reference signal.
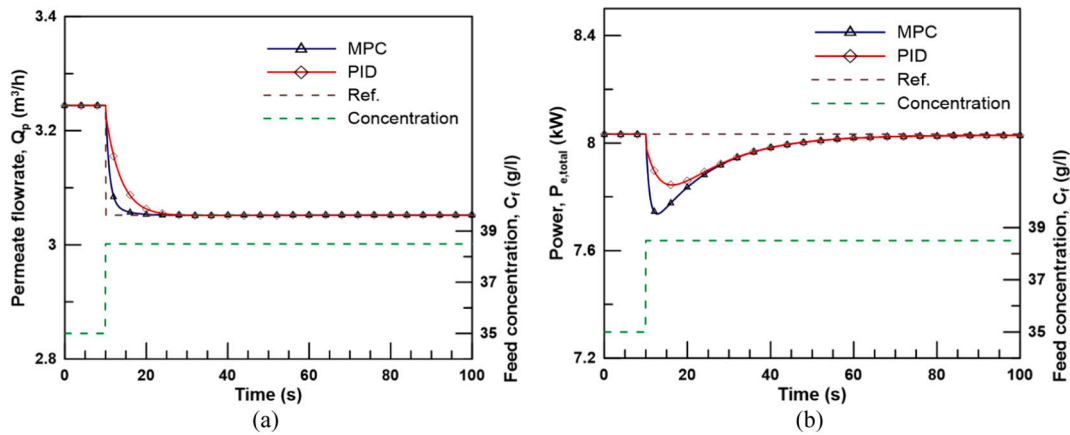

Fig. 15. Disturbance rejection test for a step-change in feed concentration presented by a) the permeate flowrate and b) the power consumption. The test is performed at a feed temperature of 25 °C.
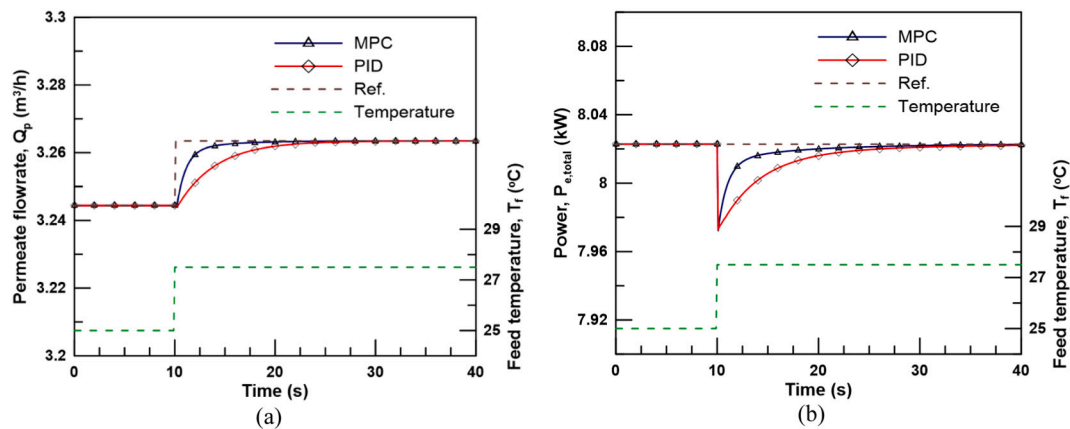

Fig. 16. Disturbance rejection test for a step-change in feed temperature presented by a) the permeate flowrate and b) the power consumption. The test is performed at a feed concentration of 35,000 mg/l.

variation scenarios.

To quantify the efficiency of the PID and MPC controllers in matching the variable reference signal, their permeate production for each scenario was compared for 1 h of operation. In all three wind speed scenarios, the MPC controller achieved higher permeate production per hour compared to the PID with varying amounts subject to wind speed

fluctuations. Fig. 20 presents the improvement percentage in hourly permeate production when the MPC controller was used compared to the PID. The results showed that with increasing wind speed disturbance, the MPC delivered improved performance compared to the PID controller, which translated to higher permeate production and better utilisation of available wind energy. The improvements in permeate

Table 6

Properties of the wind speed input and disturbance signals used for assessing the control systems performance.

Scenario	Signal type	Sample time	Mean	Standard deviation
Low wind-variation	Random signal with Gaussian distribution	10 s	6.5 m/s	0.325 m/s (5% of mean)
Medium wind-variation				0.65 m/s (10% of mean)
High wind-variation				0.975 m/s (15% of mean)
Feed concentration-variation, C_f		1 s	35,000 mg/l	700 mg/l (2% of mean)
Feed temperature-variation, T_f			25 °C	0.5 °C (2% of mean)

production per hour reached 0.31%, 1.76% and 2.35% for the low, medium, and high wind-variation scenarios, respectively. These improvements are considered a step-forward for operating RO systems with variable power, especially considering that the aim is to implement this type of control with medium to large-scale systems with capacities exceeding 40,000 m³/day [17].

6. Discussion and future work

This control-system study is unique in using a laboratory RO test rig designed to deliver similar performance to modern large-scale RO systems. The laboratory system was designed following the current industry practices of splitting the feed flow between a HPP and an isobaric pressure exchanger. The benefits of this arrangement were evident in designing the control system structure and developing the operational strategy, both of which led to outcomes different from earlier studies. The control system structure was designed based on flow control, in which the brine and permeate flowrates directly dictate the power consumption through the speed control of the pumps. This was more suitable for a system with an isobaric ERD, unlike other systems that include a throttle valve in the brine reject line and thus rely on control of the feed flowrate and feed pressure to vary the power consumption [21,23,24]. This new choice of control structure makes it more suitable for large-scale systems. As for the operational strategy, several strategies were used in previous studies to operate RO systems with variable power input [23–28]. For example, Pohl et al. [23] focussed on operation at a constant recovery, based on a RO system that uses a throttle valve in the brine reject line. In contrast, this study has shown that variable recovery at a constant brine flowrate is energy efficient when using an isobaric ERD. The ERD rotational speed is maintained constant, while only the HPP power consumption is varied to control the permeate portion of the feed flow. Maintaining a constant brine flow through the ERD also helps to avoid unstable operation of the ERD or possible increase in brine and feed mixing caused by flow variation. We therefore recommend

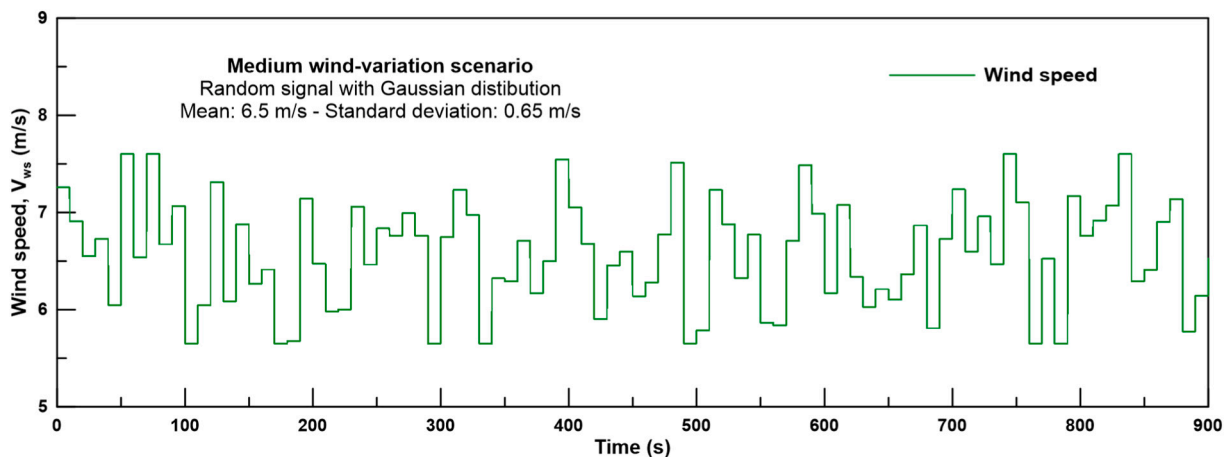**Fig. 17.** A sample of the wind speed signal used in the medium wind-variation scenario.
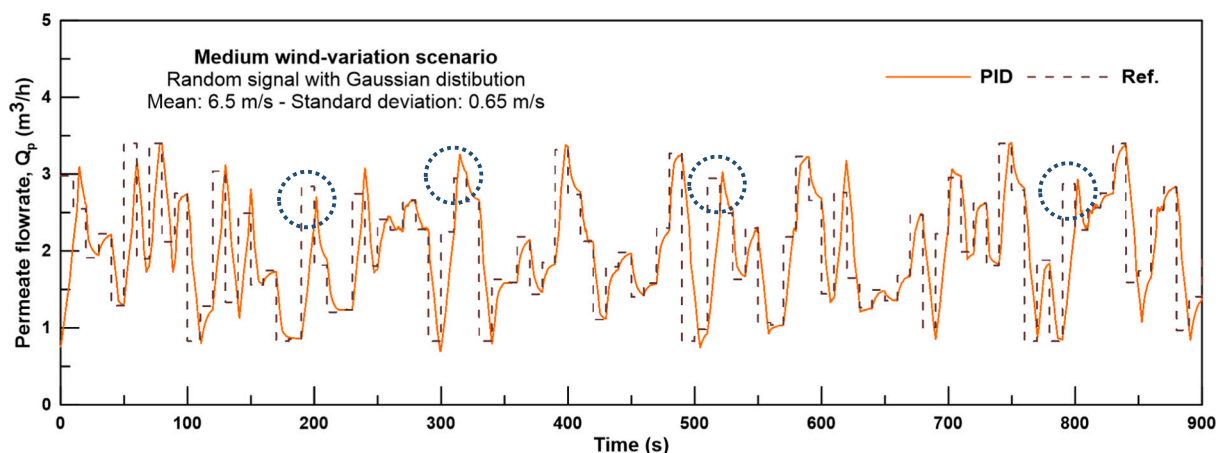

Fig. 18. Performance projection of the PID controller reference tracking capability for the input signal defined in the medium wind-variation scenario.
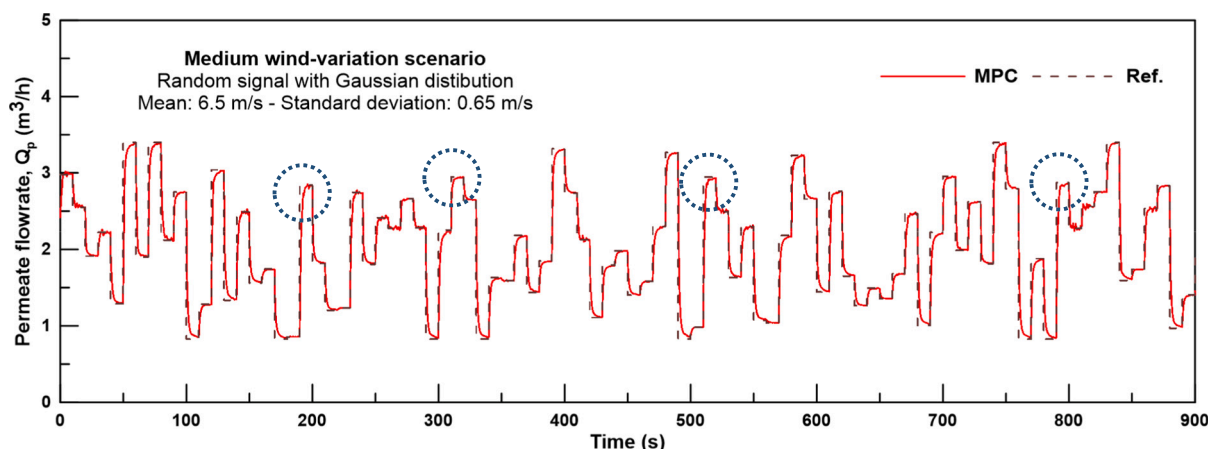
Fig. 19. Performance projection of the MPC controller reference tracking capability for the input signal defined in the medium wind-variation scenario.
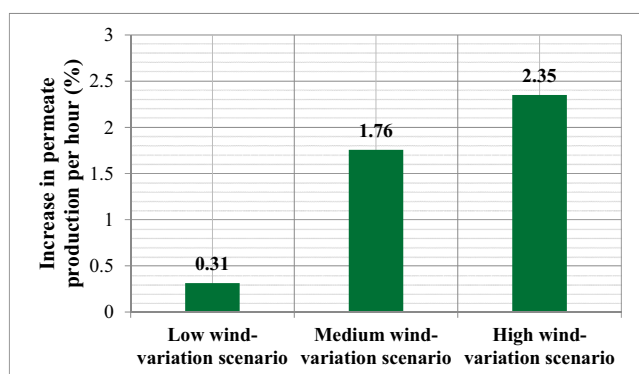

Fig. 20. Improvement in permeate production for one hour of operation due to using a model predictive controller instead of a proportional-integral-differential controller, for the three scenarios detailed in Table 6.

operating RE-powered RO systems with variable recovery at a constant brine flowrate, as it delivers the lowest specific energy consumption and widest operating range. This recommendation specifically applies to RO systems using split-feed flow configuration and an isobaric pressure exchanger, which is the current industry preference.

Furthermore, the use of MPC in RE powered-RO applications addresses a previous knowledge gap [17,24] concerning the need for advanced control systems for such applications. The MPC is an advance on the conventional PID controller, superior in maintaining the controlled output at the reference value and suppressing output variations due to disturbances. It also increases the permeate production of a RE-powered RO plant just by switching the control system design from a conventional PID to a MPC , at no additional cost. The MPC gave a 2.35% increase in permeate output for a specified wind speed scenario. This is a significant improvement, considering the target plant size. For example, applied to *Al* Khafji solar-PV powered RO plant in Saudi Arabia which has capacity of 60,000 m^3/day, this would translate to a 1410 m^3 increase in daily production [68]. If an even larger RO plant, such as Ras *Al*-Khair plant having a capacity of 1,036,000 m^3/day, were converted to variable operation using RE, the choice of using MPC over PID would boost daily production by about 24,346 m^3/day [69].

This study shows that RO systems can operate effectively and efficiently using variable power from a rapidly fluctuating RE source. However, further steps are required for the implementation of large-scale operation. First, the application of modular operation for handling RE intermittency in multi-unit RO systems should be studied [17]. Modular operation can extend operation to accommodate more widely ranging power inputs, such as diurnal solar variations. Second,

the effect of flow and pressure variation on membrane performance should be quantified for sustained periods of operation. Although the operational strategy is designed to stay within safe limits, an experimental investigation is required spanning the membrane lifetime to give a definitive conclusion on if and how the membrane performance and lifetime may be affected. Third, the possibility of using water storage instead of energy storage during periods of peak RE availability requires examination, as it has the potential to supply a consistent water demand while using RE. Furthermore, the economics of using RE for RO systems require detailed investigation in terms of the water production cost, while considering the cost of energy supplied from the grid compared to the capital and running cost of the RE system. Economic feasibility will also depend on contractual arrangements for purchasing electricity, which today is typically sold through advanced fixed-price contracts. Variable-pricing to reflect the variable availability of renewable electricity is desirable as an incentive to adopt RE-powered desalination. Finally, there is a need for intermediate-scale demonstrations, larger than the lab-scale demonstration of this paper (<100 m^3/day), but below the full-scale of modern desalination plants (>100,000 m^3/day) to identify and address risks associated with the scale up.

7. Conclusions

This study has taken a novel approach to the integration of RO and RE. An optimised variable-speed operation technique has been developed using a RO system with similar characteristics to large-scale plants. The technique defines an operational strategy that optimally varies the RO system power consumption based on rapid power input disturbances from a wind turbine with negligible rotor inertia. In addition, an advanced MPC delivering fast and robust performance has been developed to implement the optimised operational strategy. The main conclusions are:

- Feed concentration and temperature fluctuations can affect the RO system performance by altering the power consumption for the same HPP and iSave speeds. This highlights the importance of including the input disturbances in control system design and operational strategy, especially for systems subject to seasonal variations in feed water temperature and to tidal variations in feed concentration.
- Selection of an optimised operational strategy plays a crucial role in the feasibility of operating RO systems using RE. Variable recovery with constant brine flowrate yields the lowest SEC, corresponding to best utilisation of available energy, and widest operating range, allowing for permeate production at low power. This original finding applies to commercial systems using a split-feed flow configuration and isobaric pressure exchanger.

- Previous studies pointed out that a RO system operating with variable power from RE requires an advanced control system for implementation of the mapped operational strategy [17,24]. This study now shows that MPC offers superior control compared to a conventional PID controller, due to its predictive ability.
- MPC improves the settling time for a 10% step-change in permeate and brine flowrates by 47% and 92.1% respectively. Under variations in feed conditions, the MPC improves the disturbance rejection by 47.2% and 43.9% for 10% step-changes in feed concentration and temperature respectively.
- MPC improves energy utilisation compared to PID control, resulting in a 2.35% increase in hourly permeate production for a Gaussian wind speed distribution with a standard deviation of 15% about a 6.5 m/s mean. Because the change from PID to MPC requires only a software modification, this increased output incurs no extra cost.
- Using the operational strategy and control system developed, variable-speed operation can accommodate rapid fluctuations from a wind RE source to operate a RO system. The ability of the control system to accommodate the wind turbine output indicates that it will also accommodate other RE sources, such as solar, that fluctuate less rapidly.

CRediT authorship contribution statement

Mohamed T. Mito: Conceptualization, Methodology, Investigation, Formal Analysis, Original Draft, Visualisation, Review and Editing. Xianghong Ma: Review and Editing, Supervision, Resources. Hanan Albuflasa: Review and Editing, Supervision, Resources. Philip A. Davies: Conceptualization, Validation, Review and Editing, Supervision, Resources.

Declaration of competing interest

The authors declare that they have no known competing financial interests or personal relationships that could have appeared to influence the work reported in this paper.

Acknowledgements

Appendix A. Empirical equations for the feedwater properties

The feedwater properties. i.e., density (ρ), viscosity (μ) and brine diffusivity (D_B), are calculated based on the feed and brine concentration as follows [36,44]:

$$\rho = 498.4 \times m(T) + \left(248,400 \times m(T)^2 + 752.4 \times m(T) \times C_f \right)^{1/2} \tag{A.1}$$

where $m(T) = 1.0069 - 2.757 \times 10^{-4} \times T$

$$\mu = 1.234 \times 10^{-6} \times exp\left(0.0212 \times C_{bulk} + \frac{1965}{T + 273}\right) \tag{A.2}$$

$$D_B = 6.725 \times 10^{-6} \times exp\left(0.1546 \times 10^{-3} \times C_{bulk} - \frac{2513}{T + 273}\right) \tag{A.3}$$

Appendix B. Calculations for the pumps flowrate and power consumption

B.1. Low-pressure pump

Specifications of the LPP are presented in Table B.1 [70]. The pump flowrate was controlled using a modulated diaphragm valve installed on the brine reject line after the iSave. The flowrate through the LPP and control valve, Q_{LPP} (m³/s), is calculated as follows:

$$Q_{LPP} = C_v\sqrt{\frac{\Delta P_{LPP}}{SG}} \tag{B.1}$$

where ΔP_{LPP} (bar) is the differential pressure across the LPP, SG is the feed water specific gravity and C_v is the valve flow coefficient (m³/s) at the respective position. The valve operates on a linear control characteristic with a flow coefficient of 27 m³/h at the fully opened position. The inlet pressure to the pump was assumed atmospheric since an open-top feed tank was used. The flowrates through the suction and discharge ports were assumed equal by neglecting the leakage flow through the pump casing. The LPP discharge pressure is calculated through the pump curve in Table B.1. The LPP power consumption, $P_{e,LPP}$, is calculated from Eq. (B.2) based on the pump and motor efficiency.

$$P_{e,LPP} = \frac{Q_{LPP} \times \Delta p_{LPP} \times 10^2}{\eta_{p,LPP} \times \eta_{m,LPP}} \tag{B.2}$$

Table B.1
Low-pressure pump specifications.

Pump	Type	LOWARA CEA210/5/D-V	
	Maximum flowrate (Q_{LPP})	18 m³/h	
	Efficiency ($\eta_{p,\,LPP}$)	0.53%	
Pump curve	Q_{LPP} = 7.2 m³/h	Q_{LPP} = 12 m³/h	Q_{LPP} = 18 m³/h
	ΔP_{LPP} = 2.82 bar	ΔP_{LPP} = 2.66 bar	ΔP_{LPP} = 2.31 bar
Motor	Power ($P_{e,LPP}$)	2.2 kW	
	Efficiency ($\eta_{m,\,LPP}$)	0.85%	
	Pole ($N_{p,LPP}$)	2	

B.2. High-pressure pump

Specifications of the HPP are presented in Table B.2 [32]. The pump flowrate is directly proportional to the shaft speed regardless of discharge pressure. The pump pressure differential, ΔP_{HPP}, is the difference between the RO feed pressure and the LPP supply pressure. The pump was controlled using a VFD that varies the supply frequency and voltage to proportionally control the rotational speed. The pump's rotational speed N_{HPP} is calculated as follows:

$$N_{HPP} = \frac{120 F_{HPP}}{N_{p,HPP}} \tag{B.3}$$

where F_{HPP} is the VFD supply frequency and $N_{p,HPP}$ is the number of poles of the induction motor. Accordingly, the flowrate supplied by the pump Q_{HPP} is calculated from Eq. (B.4) based on the volumetric displacement $V_{d,HPP}$, assuming no leakage losses in the pump casing.

$$Q_{HPP} = V_{d,HPP} \times \frac{N_{HPP}}{60} \tag{B.4}$$

The shaft power transmitted by the HPP motor, $P_{shaft,HPP}$, is calculated from Eq. (B.5), which is an empirical formula provided by the pump's manufacturer. The HPP power consumption, $P_{e,HPP}$, is calculated from Eq. (B.6) based on shaft power and motor efficiency.

$$P_{shaft,HPP} = \frac{16.7 \times Q_{HPP} \times 3600 \times \Delta P_{HPP}}{530} \tag{B.5}$$

$$P_{e,HPP} = \frac{P_{shaft,HPP}}{\eta_{m,HPP}} \tag{B.6}$$

Table B.2
High-pressure pump specifications.

	Type	Danfoss APP 3.5		
Pump	Maximum flowrate (Q_{HPP})	3.5 m³/h		
	Volumetric displacement ($V_{d,HPP}$)	20.54×10^{-6} m³/rev		
	Power ($P_{e,HPP}$)	11 kW		
Motor	Efficiency ($\eta_{m,\,HPP}$)	1/1 load	3/4 load	1/2 load
		92.5%	92.7%	90.9%
	Pole ($N_{p,HPP}$)	2		

B.3. Energy recovery device (iSave)

Specifications of the Danfoss iSave are shown in Table B.3 [33]. The iSave's motor was controlled using a VFD for flow control. The iSave's motor speed, N_{iSave}, is calculated from Eq. (B.7), such that F_{iSave} is the supply frequency and $N_{p,iSave}$ is the number of poles of the induction motor. The flowrate through the iSave is calculated based on the volumetric displacement, $V_{d,iSave}$, from Eq. (B.8).

$$N_{iSave} = \frac{120 F_{iSave}}{N_{p,iSave}} \tag{B.7}$$

$$Q_{iSave} = V_{d,iSave} \times \frac{N_{iSave}}{60} \tag{B.8}$$

The iSave power consumption $P_{e,iSave}$ is calculated from Eq. (B.9) based on the shaft torque τ_{shaft}, the motor efficiency $\eta_{m,\,iSave}$ and the rotational velocity ω (rad/s). The shaft torque and motor efficiency are presented in the iSave's datasheet [33].

$$P_{e,isave} = \frac{\tau_{shaft} \times \omega}{\eta_{m,iSave}} \tag{B.9}$$

The lubrication flow for the iSave is presented based on the iSave flowrate Q_{iSave} and the brine pressure P_b in Fig. B.1 [33]. Slight mixing occurs between the brine and seawater streams due to the lack of a physical barrier between them [40]. The increase in feed concentration can be estimated

by calculating the outlet feed salinity from the mixing percentage as follows [71]:

$$Mixing\ (\%) = \frac{C_{iSave} - C_f}{C_b - C_f} \times 100 \tag{B.10}$$

where C_{iSave} is the concentration of the High-pressure (HP) feed leaving the iSave, C_f is the feedwater concentration and C_b is the HP brine concentration. The mixing volume is primarily subject to the flow balance between the HP and LP ducts of the pressure exchanger. The iSave was assumed to be operating with a balanced flow to minimise calculations, at which the volumetric mixing is estimated at 5% [33].

Table B.3
Energy recovery device specifications [33].

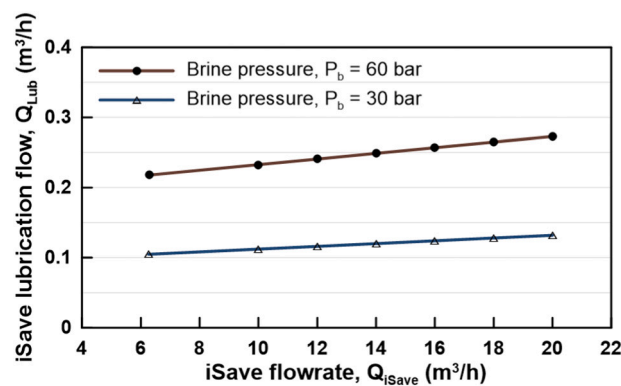|	Type	Danfoss iSave 21 Plus		
Pump	Flowrate (Q_{iSave})	6–22 m³/h		
	Volumetric displacement ($V_{d,iSave}$)	273×10^{-6} m³/rev		
	Power ($P_{e,iSave}$)	5.5 kW		
Motor	Efficiency ($\eta_{m,\ iSave}$)	1/1 load	3/4 load	1/2 load
		87.7%	88.2%	87.1%
	Pole ($N_{p,iSave}$)	4		

Fig. B.1. Lubrication flow required to lubricate the iSave moving parts.

Appendix C. Supplementary data

Supplementary data to this article can be found online at https://doi.org/10.1016/j.desal.2022.115715.

References

[1] UN-Habitat, World Cities Report, 2016.

[2] UN, UN sustainable development goals. 06/03/20, Available from: https://www.un.org/sustainabledevelopment/water-and-sanitation/, 2021 May.

[3] E. Jones, et al., The state of desalination and brine production: a global outlook, Sci. Total Environ. 657 (2019) 1343–1356.

[4] N. Voutchkov, Energy use for membrane seawater desalination – current status and trends, Desalination 431 (2018) 2–14.

[5] IDA, IDA Desalination Yearbook 2017–2018, 2017.

[6] M.A. Abdelkareem, et al., Recent progress in the use of renewable energy sources to power water desalination plants, Desalination 435 (2018) 97–113.

[7] M.W. Shahzad, et al., Energy-water-environment nexus underpinning future desalination sustainability, Desalination 413 (2017) 52–64.

[8] M.T. Mito, P. Davies, Towards energy-efficient reverse osmosis, in: A. Sapalidis (Ed.), Membrane Desalination From Nanoscale to Real World Applications, Taylor & Francis Group, New York, 2020, pp. 303–324.

[9] U. Caldera, D. Bogdanov, C. Breyer, Chapter 8 - desalination costs using renewable energy technologies, in: V.G. Gude (Ed.), Renewable Energy Powered Desalination Handbook, Butterworth-Heinemann, 2018, pp. 287–329.

[10] A. Ali, et al., Membrane technology in renewable-energy-driven desalination, Renew. Sust. Energ. Rev. 81 (2018) 1–21.

[11] B. Peñate, et al., Assessment of a stand-alone gradual capacity reverse osmosis desalination plant to adapt to wind power availability: a case study, Energy 36 (7) (2011) 4372–4384.

[12] V.G. Gude, Energy storage for desalination processes powered by renewable energy and waste heat sources, Appl. Energy 137 (2015) 877–898.

[13] E.S. Mohamed, et al., A direct coupled photovoltaic seawater reverse osmosis desalination system toward battery based systems — a technical and economical experimental comparative study, Desalination 221 (1–3) (2008) 17–22.

[14] H. Qiblawey, F. Banat, Q. Al-Nasser, Laboratory setup for water purification using household PV-driven reverse osmosis unit, Desalin. Water Treat. 7 (1–3) (2009) 53–59.

[15] C. Abbey, G. Joos, Supercapacitor energy storage for wind energy applications, IEEE Trans. Ind. Appl. 43 (3) (2007) 769–776.

[16] H. Sharon, K.S. Reddy, A review of solar energy driven desalination technologies, Renew. Sust. Energ. Rev. 41 (2015) 1080–1118.

[17] M.T. Mito, et al., Reverse osmosis (RO) membrane desalination driven by wind and solar photovoltaic (PV) energy: state of the art and challenges for large-scale implementation, Renew. Sust. Energ. Rev. 112 (2019) 669–685.

[18] V.J. Subiela, J.A. Carta, J. González, The SDAWES project: lessons learnt from an innovative project, Desalination 168 (2004) 39–47.

[19] M.T. Mito, Prospects of wind power prediction and variable operation in optimizing wind-powered reverse osmosis operation, in: International Desalination Association. World Congress on Desalination and Water Reuse 2019, Crossroads to Sustainability, International Desalination Association (IDA), Dubai, United Arab Emirates, 2019.

[20] A.A. Abufayed, Performance characteristics of a cyclically operated seawater desalination plant in Tajoura, Libya, Desalination 156 (2003) 59–65.

[21] W. Khiari, M. Turki, J. Belhadj, Power control strategy for PV/Wind reverse osmosis desalination without battery, Control. Eng. Pract. 89 (2019) 169–179.

[22] M.S. Miranda, D. Infield, A wind powered seawater reverse-osmosis system without batteries, Desalination 153 (2002) 9–16.

[23] R. Pohl, M. Kaltschmitt, R. Holländer, Investigation of different operational strategies for the variable operation of a simple reverse osmosis unit, Desalination 249 (3) (2009) 1280–1287.

[24] J.A. Carta, et al., Preliminary experimental analysis of a small-scale prototype SWRO desalination plant, designed for continuous adjustment of its energy consumption to the widely varying power generated by a stand-alone wind turbine, Appl. Energy 137 (2015) 222–239.

[25] S. Loutatidou, et al., Wind-powered desalination for strategic water storage: techno-economic assessment of concept, Desalination 408 (2017) 36–51.

[26] S. Kumarasamy, S. Narasimhan, S. Narasimhan, Optimal operation of battery-less solar powered reverse osmosis plant for desalination, Desalination 375 (2015) 89–99.

[27] B.S. Richards, et al., Renewable energy powered membrane technology: safe operating window of a brackish water desalination system, J. Membr. Sci. 468 (2014) 400–409.

[28] M. Thomson, D. Infield, Laboratory demonstration of a photovoltaic-powered seawater reverse-osmosis system without batteries, Desalination 183 (1) (2005) 105–111.

[29] L.G. Palacın, Modelling, Simulation and Advanced Control of Small Scale Reverse Osmosis Desalination Plants, University of Valladolid, 2014.

[30] W. Lai, et al., Effects of wind intermittence and fluctuation on reverse osmosis desalination process and solution strategies, Desalination 395 (2016) 17–27.

[31] A.M. Bilton, L.C. Kelley, S. Dubowsky, Photovoltaic reverse osmosis — feasibility and a pathway to develop technology, Desalin. Water Treat. 31 (1–3) (2012) 24–34.

[32] Danfoss, Danfoss APP pumps [cited 2021 May]; Available from: https://www.danfoss.com/en-gb/products/hpp/pumps/high-pressure-pumps-for-reverse-osmosis-applications/app-pumps/, 2021.

[33] Danfoss, Danfoss iSave 21 plus [cited 2021 April]; Available from: https://www.danfoss.com/en/products/energy-recovery-devices/hpp/energy-recovery-devices-for-reverse-osmosis-applications/isave-21-plus/#tab-overview/, 2021.

[34] J.G. Wijmans, R.W. Baker, The solution-diffusion model: a review, J. Membr. Sci. 107 (1995) 1–21.

[35] S. Kim, E.M.V. Hoek, Modeling concentration polarization in reverse osmosis processes, Desalination 186 (1) (2005) 111–128.

[36] J.S. Kim, J. Chen, H.E. Garcia, Modeling, control, and dynamic performance analysis of a reverse osmosis desalination plant integrated within hybrid energy systems, Energy 112 (2016) 52–66.

[37] M.A. Al-Obaidi, I.M. Mujtaba, Steady state and dynamic modeling of spiral wound wastewater reverse osmosis process, Comput. Chem. Eng. 90 (2016) 278–299.

[38] DUPONT, FilmTec SW30HRLE-400 element data sheet [cited 2021 April]; Available from: https://www.dupont.com/content/dam/dupont/amer/us/en/water-solutions/public/documents/en/45-D00967-en.pdf, 2021.

[39] S.A. Avlonitis, M. Pappas, K. Moutesidis, A unified model for the detailed investigation of membrane modules and RO plants performance, Desalination 203 (1–3) (2007) 218–228.

[40] V. Pikalov, et al., Demonstration of an energy recovery device well suited for modular community-based seawater desalination systems: result of danfoss iSAVE 21 testing, Desalin. Water Treat. 51 (22–24) (2013) 4694–4698.

[41] DUPONT , FILMTEC - Reverse Osmosis Membranes - Technical Manual.

[42] J. Kim, K. Park, S. Hong, Application of two-stage reverse osmosis system for desalination of high-salinity and high-temperature seawater with improved stability and performance, Desalination 492 (2020), 114645.

[43] K. Park, et al., Design, modelling and optimisation of a batch reverse osmosis (RO) desalination system using a free piston for brackish water treatment, Desalination 494 (2020), 114625.

[44] C. Koroneos, A. Dompros, G. Roumbas, Renewable energy driven desalination systems modelling, J. Clean. Prod. 15 (5) (2007) 449–464.

[45] D. Van Gauwbergen, J. Baeyens, Macroscopic fluid flow conditions in spiral-wound membrane elements, Desalination 110 (3) (1997) 287–299.

[46] R. Energy, E-10 HAWT - 10kW small wind turbine for on-grid & off-grid power systems [cited 2021 March]; Available from: https://www.ryse.energy/10kw-wind-turbines/, 2021.

[47] A. Gambier, Dynamic modelling of the rotating subsystem of a wind turbine for control design purposes, IFAC PapersOnLine 50 (2017) 9896–9901.

[48] M. Thomson, Reverse-osmosis desalination of seawater powered by photovoltaics without batteries, Loughborough University, 2003. https://dspace.lboro.ac.uk/2134/10701.

[49] A. Abbas, Model predictive control of a reverse osmosis desalination unit, Desalination 194 (1–3) (2006) 268–280.

[50] A. Kiam Heong, G. Chong, L. Yun, PID control system analysis, design, and technology, IEEE Trans. Control Syst. Technol. 13 (4) (2005) 559–576.

[51] D.T. Korsane, V. Yadav, K.H. Raut, PID tuning rules for first order plus time delay system, Int. J. Innov. Res. Electr. Electron. Instrum. Control Eng. 2 (1) (2014).

[52] R. Sen, et al., Comparison between three tuning methods of PID control for high precision positioning stage, J. Metrol. Soc. India 30 (1) (2014) 65–70.

[53] T. Nagy, Flexible and efficient solution for control problems of chemical laboratories, in: A.A. Kiss (Ed.), Computer Aided Chemical Engineering, Elsevier, 2019, pp. 1819–1824.

[54] W. Zhao, et al., Implement and performance comparison of three turning methods of PI controller parameters for buck converter based on MATLAB/Simulink, IET Conf. Proc. (2021) 982–989.

[55] MathWorks, PID tuner [cited 2021 September]; Available from: https://www.mathworks.com/help/control/ref/pidtuner-app.html, 2021.

[56] Danfoss, Danfoss iSave 21 - installation, operation and maintenance manual [cited 2021 April]; Available from: https://www.danfoss.com/en/products/hpp/energy-recovery-devices/energy-recovery-device-for-small-to-medium-swro-applications/isave-21-plus/, 2021.

[57] S.J. Qin, T.A. Badgwell, A survey of industrial model predictive control technology, Control. Eng. Pract. 11 (7) (2003) 733–764.

[58] C.E. Garcia, D.M. Prett, M. Morari, Model predictive control: theory and practice - a survey, Automatica 25 (1989) 335–348.

[59] C. Cutler, B.L. Ramaker, Dynamic matrix control??A computer control algorithm, in: Joint Automatic Control Conference, 1980, p. 72. San Francisco, CA.

[60] P. Lundström, et al., Limitations of dynamic matrix control, Comput. Chem. Eng. 19 (4) (1995) 409–421.

[61] D.M. Prett, C.E. García, in: D.M. Prett, C.E. García (Eds.), Fundamental Process Control, Butterworth-Heinemann, 1988, pp. 1–5.

[62] J.P. Torreglosa, et al., Energy dispatching based on predictive controller of an off-grid wind turbine/photovoltaic/hydrogen/battery hybrid system, Renew. Energy 74 (2015) 326–336.

[63] A. Bemporad, M. Morari, N.L. Ricker, Model Prediditive Control Toolbox: User's Guide, MathWorks, 2014.

[64] L. Ljung, Perspectives on system identification, Annu. Rev. Control. 34 (1) (2010) 1–12.

[65] D.E. Seborg, T.F. Edgar, D.A. Mellichamp, Process Dynamics and Control, Wiley, 2004.

[66] P.R. Maurath, et al., Predictive controller design by principal components analysis, Ind. Eng. Chem. Res. 27 (7) (1988) 1204–1212.

[67] M.F.A. Goosen, et al., Effect of feed temperature on permeate flux and mass transfer coefficient in spiral-wound reverse osmosis systems, Desalination 144 (1) (2002) 367–372.

[68] F.E. Ahmed, R. Hashaikeh, N. Hilal, Solar powered desalination – technology, energy and future outlook, Desalination 453 (2019) 54–76.

[69] A. Bennett, Advances in desalination energy recovery, World Pumps 2015 (7) (2015) 30–34.

[70] Xylem, LOWARA CEA - end suction centrifugal pumps [cited 2021 May]; Available from: https://www.xylem.com/en-uk/brands/lowara/lowara-products/cea-stainless-steel-threaded-centrifugal-pumps/, 2021.

[71] R.L. Stover, Seawater reverse osmosis with isobaric energy recovery devices, Desalination 203 (1–3) (2007) 168–175.